a RADICAL look at STARBURST galaxies

modeling the dusty cores of starburst ULIRGs

A.F. Loenen[1]
supervision: W.A. Baan[2] and M. Spaans[1]

[1] Kapteyn Astronomical Institute, P.O. Box 800, 9700 AV Groningen, the Netherlands
[2] ASTRON, P.O. Box 2, 7990 AA Dwingeloo

1. Introduction

In 1983 the Infra-Red Astronomical Satellite (IRAS) surveyed 96% of the sky in four broad-band filters at 12μm, 25μm, 60μm, and 100μm. IRAS detected infrared (IR) emission from about 25,000 galaxies, primarily from spirals, but also from quasars (QSOs), Seyfert galaxies and early type galaxies. Among these galaxies IRAS discovered a new class of galaxies that radiate most of their energy in the infrared. The most luminous of these infrared galaxies, the (ultra-)luminous infrared galaxies [(U)LIRGs], have QSO-like luminosities of L $\geq 10^{11}$ L$\odot$ (LIRGs) or even L $\geq 10^{12}$ L$\odot$ (ULIRGs) (Genzel & Cesarsky, 2000).

Despite extensive observations over the last decades, the central questions regarding the source of the large IR luminosity of ULIRGs, and their evolution, are still not fully answered. Sanders et al. (1988) proposed that most ULIRGs are powered by dust-enshrouded QSOs in the late phases of a merger. The final state of such a merger would be a large elliptical galaxy with a massive quiescent black hole at its center (Kormendy & Sanders, 1992). A significant fraction of the ULIRG population seems to confirm this assumption, since they exhibit nuclear optical emission line spectra similar to those of Seyfert galaxies (Sanders et al., 1988). Some also contain compact central radio sources and highly absorbed, hard X-ray sources, all indicative of an active nucleus (AGN).

On the other hand, the IR, mm, and radio characteristics of ULIRGs are similar to those of starburst galaxies. A centrally condensed burst of star formation activity, fueled by gas driven into the center of the potential well of a pair of interacting galaxies by bar instability provides an equally plausible power source (Blain et al., 2002). Observational evidence for the starburst nature of ULIRGs was found with the detection of a number of compact radio hypernovae in each of the two nuclei of Arp 220 by Smith et al. (1998).

In ULIRGs that are at sufficiently low redshift for their internal structure to be resolved, the great majority of the IR emission is found to originate from sub-kpc dusty region within merging systems of galaxies (e.g. Downes & Solomon, 1998). These dusty starburst galaxies are an important class of objects. About 25% of the high-mass star formation within 10 Mpc occurs in just four starburst galaxies (M82, NGC 253, M83, NGC 4945; Heckman, 1998). Even though these galaxies create vast amounts of stars, the time scale of this formation is short. Near-IR imaging spectroscopy in M82, IC 342, and NGC 253 indicates that in the evolution these galaxies, there are several episodes of star formation activity, with timescales of around 10^7 to 10^8 years (Genzel & Cesarsky, 2000). In these short period they produce a vast amount of stars. The relatively low efficiency of the energy production of stars ($E \sim 10^{-3} M_\star c^2$) and the large energy output (up to $\sim 10^{61}$ ergs for a ultraluminous starburst like ARP 220) yield a production 10^8 to 10^{10} M$\odot$ of stars per burst. Combined with the short timescales, this leads to a star formation rate (SFR) of 10 to 100 M$\odot$ per year (Heckman, 1998).

The goal of this paper is to present a model for these dust-enshrouded star formation regions and to study and explain the behavior of the IR properties of starburst ULIRGs during their evolution. The model consists of a number of existing models and codes, which are combined into one.

The structure of this paper is as follows: in section 2 the models and the theory behind them are discussed. The parameter space and the simulations are discussed in section 3 and the results of these simulations in section 4. In the last section the results are discussed and some suggestions for future work are made.

2. The model

In figure 1 the "physical" setup of our model is shown. In the center of our model a star formation region is placed. That starburst is surrounded by a dusty environment, which is responsible for the emission of the IR ra-

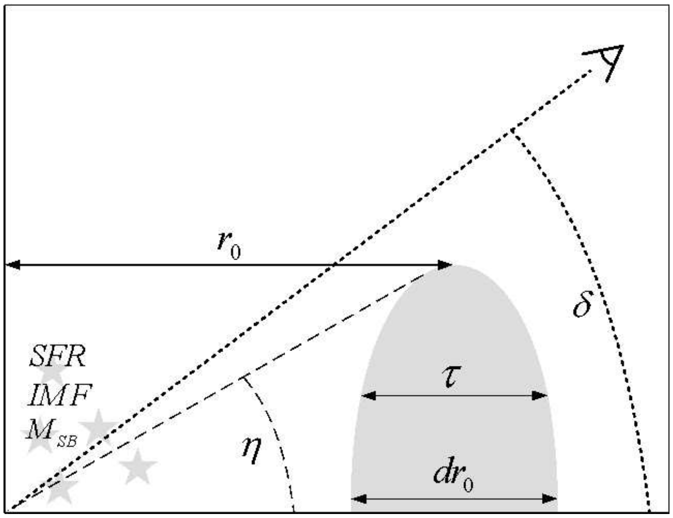

Fig. 1. Schematic overview of the "physical" environment created in the simulations. In the center star formation is going on, which radiates the dusty surroundings (here represented as a toroidal shape). This dust then radiates its given energy in the IR regime. Also the parameter space is shown. In the starburst, the total stellar mass $M_{\rm SB}$, the star formation rate (SFR) and the IMF-slope α are varied. In the dust the geometry is varied by changing the closing angle η. Also the dust density (or optical depth τ)is varied. A last variable is the observational inclination δ. Also some parameters are shown, which were not varied: the radius r and the radial scale size dr. More information on the parameter space can be found in section 3.

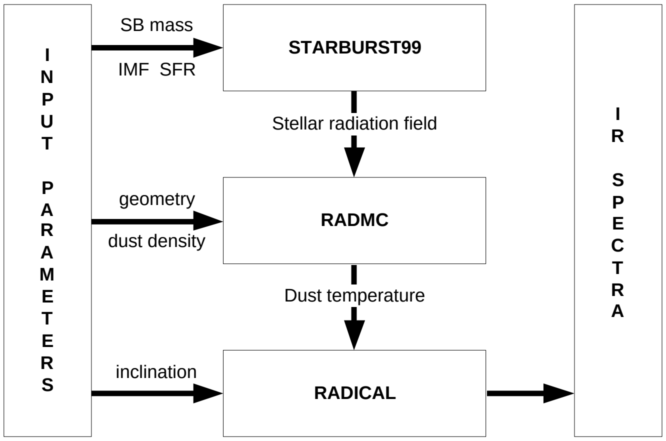

Fig. 2. This flowchart shows the computational setup. As can be seen, first the starburst properties are calculated using STARBURST99 (section 2.1) and the results of these calculations are used as input for the dust calculations, which are performed by RADMC and RADICAL (sections 2.2 and 2.3).

diation. Figure 2 shows the computational setup of the model. The computations are organized in roughly the same way as the physical environment: first the spectral energy distribution (SED) of the star formation region is calculated using STARBURST99 (see section 2.1). This SED is then used as input spectrum for the radiative transport calculations in the dusty environment. These calculations are done by RADMC and RADICAL (see sections 2.2 and 2.3). RADMC calculates the dust temperature and RADICAL does the ray-tracing which provides the emergent IR spectrum. This sequence of calculations is repeated for every time step.

2.1. STARBURST99

As mentioned above, the stellar properties of the starburst are calculated using STARBURST99[1] (hereafter SB99), which is a set of stellar models, optimized to reproduce properties of galaxies with active star formation and their evolution through time. In this paper only a brief summary of the model will be given. More information on the entire set can be found in Leitherer et al. (1999). Detailed information on the computational techniques can be found in Leitherer et al. (1992) and Leitherer & Heckman (1995).

The calculation can roughly be divided into three stages. First an ensemble of stars is formed and distributed along the zero-age main sequence (ZAMS). This distribution is determined by the available gas mass and the initial mass function (IMF). Another crucial parameter is whether the star formation is continuous (i.e., the duration of the starburst is long compared to the evolution time scale of the stars) or concentrated in one instantaneous burst (i.e., the duration is short compared to the evolution). If the star formation is continuous stars keep forming according to the (constant) star formation rate (SFR). In the case of one burst, all the available gas is transformed into stars instantaneously at the beginning of the simulation. These cases are the two extremes of star formation and realistic models will, therefore, lie in between these two limits (Leitherer & Heckman, 1995; Leitherer et al., 1992).

After the stars have been distributed, evolutionary models describe the time dependence of the stellar properties, such as stellar mass, luminosity, spectra, effective temperature, and chemical composition. These models are calculated with the so-called isochrone synthesis method. Isochrone synthesis was introduced by Charlot & Bruzual (1991) as a method to overcome the discrete appearance of the model predictions at late evolutionary stages. Instead of binning the stars by mass and assigning them to an evolutionary track as was done in codes previous to SB99 (Leitherer et al., 1992; Leitherer & Heckman, 1995), continuous isochrones are calculated by interpolating between tracks in the Herzsprung-Russel diagram (HRD) on a variable mass grid. The stellar properties are calculated by interpolating between points on the grids of pre-calculated models. These models are based on the evolutionary tracks for enhanced mass loss of Meynet et al. (1994) and the model atmosphere grid compiled by Lejeune et al. (1997), supplemented by the pure helium Wolf-Rayet (WR) atmospheres of Schmutz et al. (1992). Smith et al. (2002) provided the fully line-blanketed WR model atmospheres and non-LTE O-star atmospheres (Leitherer et al., 1999). The properties obtained from interpolation are the starting points of the next step of the evolution. This iterative process is repeated for all time steps.

---

[1] The code and pre-calculated data sets are publicly available at http://www.stsci.edu/science/starburst99/

In the last stage the integrated properties of the star formation region are calculated by determining the stellar number densities in the HRD, assigning all the properties to these stars and integrating over the entire population (Leitherer & Heckman, 1995).

2.2. RADMC

The output SEDs of the SB99 calculations are used to "feed" the dusty environment. In order to do this the SB99 spectrum is re-binned to the number of channels available in the dust simulation codes. The re-binning is performed in such a way that the 10μm, 20μm, 60μm and 100μm bands are included, so that the resulting IR data can be compared to IRAS observations[2].

The physical dust environment is simulated by creating a dust density grid with a central cavity. This cavity is the region surrounding the central starburst in which the dust and gas are destroyed and blown away by the star formation activity. Since we also want to explore the influence of the dust geometry on the emergent SEDs in our simulations, a 3D grid is needed. This, however, would lead to large calculation times. In order to limit this problem, the grid is chosen to be axisymmetric. This way the grid is reduced to 2D again, but still allows for various astrophysically interesting dust distributions, like shells, tori and disks.

RADMC[3] is a 2-D Monte-Carlo radiative transfer code for axisymmetric circumstellar disks and envelopes. It is based on the method of Bjorkman & Wood (2001), but with several modifications to produce smoother results with fewer photon packages.

The method introduced by Bjorkman & Wood (2001) is to divide the luminosity of the radiation source L (in this case the re-binned output spectrum of SB99) into N_γ equal-energy, monochromatic "photon packets" that are emitted stochastically by the source over a time interval Δt. Each photon packet then has energy E_γ, so

$$E_\gamma = \frac{L\Delta t}{N_\gamma} \ . \tag{1}$$

Note that since the packets have equal energy, the number of actual photons in each packet changes with frequency. The frequencies of the packets are randomly chosen, with a distribution corresponding to the input SED. This frequency determines the dust absorption opacity (κ_ν), the scattering opacity (σ_ν) and the scattering parameters of the random walk of the packet through the grid. After they are emitted, the packets are traced to random interaction locations on the dust grid, determined by the dust density distribution. There they are either scattered or absorbed with a probability given by the albedo. If the packet is scattered, a random scattering angle is chosen and the packet is traced to the next interaction location. If instead the packet is absorbed, its energy is added to the grid cell, raising the temperature of the cell. In every iteration step, the number of absorbed packets in each cell (N_i, where i is the cell index) is recorded, and the total absorbed energy then is

$$E_i^{\rm abs} = N_i E_\gamma \ . \tag{2}$$

In order to ensure energy conservation and radiative equilibrium, the absorbed packets must be re-emitted immediately. Their new frequencies are determined by the new grid cell temperature. Local thermal equilibrium (LTE) is assumed, so the amount of emitted energy equals $E_i^{\rm abs}$. The thermal emissivity of the dust $j_\nu = \rho\kappa_\nu B_\nu(T)$, where ρ is the dust density and $B_\nu(T)$ is the Planck function at temperature T , so the emitted energy is

$$\begin{aligned} E_i^{\rm em} &= 4\pi\Delta t \iint j_\nu {\rm d}\nu {\rm d}V_i \\ &= 4\pi\Delta t \iint \rho\kappa_\nu B_\nu(T) {\rm d}\nu {\rm d}V_i \\ &= 4\pi\Delta t \int \rho\kappa_P(T) B(T) {\rm d}V_i \ , \end{aligned} \tag{3}$$

where V_i is the volume of the cell, $\kappa_P(T) = \int \kappa_\nu B_\nu(T){\rm d}\nu / B(T)$ is the Planck mean opacity and $B(T) = \sigma T^4/\pi$ is the frequency integrated Planck function. If the temperature is assumed constant in the entire cell (T_i), then

$$E_i^{\rm em} = 4\pi\Delta t \, \kappa_P(T_i) B(T_i) \, m_i \ , \tag{4}$$

where m_i is the mass of the dust in the cell. The new dust temperature, after the absorption of N_i packets, can be obtained by equating the absorbed (eq. (2)) and emitted (eq. (4)) energies:

$$\sigma T_i^4 = \frac{N_i L}{4 N_\gamma \kappa_P(T_i) m_i} \ . \tag{5}$$

Since the Planck mean opacity κ_P is a function of temperature, equation (5) is an implicit equation for the temperature, which must be solved every time a packet is absorbed. Since the number of packets is high ($N = 10^5$), this equation has to be solved many times. Therefore, an efficient algorithm is desirable. Fortunately, κ_P is a slowly varying function of temperature, and so equation (5) can be solved using a relatively simple iterative algorithm. For this algorithm, the Planck mean opacities are precalculated for a large range of temperatures. The required opacity is then interpolated using the previous temperature. This results in a new temperature estimate, which is inserted into the next iteration step. This way T_i can be solved in only a few iterations. Now that the new cell temperature is known, the excess energy can be re-radiated. The new emissivity is $j_\nu = \rho\kappa_\nu B_\nu(T_i)$ and the emissivity of the cell before heating was $j'_\nu = \rho\kappa_\nu B_\nu(T_i - \Delta T)$, where ΔT is the temperature difference. Thus, the correction of

---

[2] In the SB99 output SED, 12 and 25 μm are not available. Instead 10 and 20 μm are used.

[3] For more information on the RADMC, its availability and related publications see http://www.mpia-hd.mpg.de/homes/dullemon/radtrans/radmc/

the emissivity, needed to radiate away the excess energy, is

$$\Delta j_\nu = j_\nu - j'_\nu = \rho\kappa_\nu \left[B_\nu(T_i) - B_\nu(T_i - \Delta T)\right] \ . \tag{6}$$

Since the number of photon packets is large, the energy of the packets (E_γ) is low, leading to a small temperature change ΔT. The emissivity correction then reduces to

$$\Delta j_\nu = \rho\kappa_\nu \Delta T \left(\mathrm{d}B_\nu/\mathrm{d}T\right) \ . \tag{7}$$

The shape of this function determines the distribution from which a random new frequency is chosen. With this new frequency the packet's new scattering and absorption parameters are determined, and the packet is re-emitted.

After either being scattered or absorbed and re-emitted, the photon packet continues to a new interaction location. This process is repeated until all the packets escape the dusty environment. Because all the injected packets eventually escape, so does all the injected energy and therefore, the total energy is automatically conserved. Another advantage of this approach is that the simulation does not have some sort of convergence criterion to meet, so the only source of error in the calculation is the statistical error inherent to Monte Carlo simulations.

The problem with the Bjorkman & Wood method is that it produces very noisy temperature profiles in regions of low optical depth, and requires a large number of photons ($N \sim 10^7$) for a smooth SED. These disadvantages have been solved in RADMC by treating absorption partly as a continuous process (see Lucy 1999 for more information), and using the resulting smooth temperature profiles with a separate ray-tracing code (RADICAL) to produce images and SEDs. These images and SEDs have a low noise level even for relatively few photon packages ($N \sim 10^5$). This improved Bjorkman & Wood method works well at all optical depths, but may become slow in cases where the optical depth is very large (Pascucci et al., 2004), but these high optical depths ($\tau_\nu \sim 1000$) are not reached in our simulations.

2.3. RADICAL

As mentioned in the previous section, RADMC produces a dust temperature grid. This grid, combined with the SED of the central source, is used by RADICAL[4] to produce the final spectra. RADICAL is a lambda operator subroutine (using the MALI scheme of Rybicki & Hummer 1991) based on the method of "Short Characteristics", implemented on a polar grid by Dullemond & Turolla (2000)[5]. It solves the radiative transfer equation (RTE) on the entire grid, using the dust temperature to calculate the source function.

The formal RTE is

$$\frac{\mathrm{d}I_\nu}{\mathrm{d}s} = \alpha_\nu \left(S_\nu - I_\nu\right) \ , \tag{8}$$

where I_ν is the intensity, S_ν the source function, α_ν the opacity and s the path length. This equation must hold along every path, i.e. every straight line through the medium. In its integral form it gives the intensity for a ray through a point P:

$$I_\nu(P) = e^{-\tau_\nu} I_\nu(0) + \int_0^{\tau_\nu} e^{-\tau'_\nu} S(\tau'_\nu)\mathrm{d}\tau'_\nu \ , \tag{9}$$

where τ_ν is the optical depth along the ray, between P and the edge of the medium. The mean intensity J_ν can be calculated by averaging over all angles ω

$$J_\nu = \frac{1}{4\pi} \int I_\nu(\omega)\mathrm{d}\omega \ . \tag{10}$$

This mean intensity needs to be calculated for every point P on the grid. For a given source function S_ν this can be written as a linear Lambda Operation Λ:

$$J_\nu = \Lambda \left[S_\nu\right] \ . \tag{11}$$

The transfer equation for thermal emission and isotropic dust scattering can then be written as:

$$S_\nu = \epsilon B_\nu(T) + (1-\epsilon)\Lambda[S_\nu] \ , \tag{12}$$

where $\epsilon \equiv \alpha_\nu^{\mathrm{abs}}/\alpha_\nu$ is the thermalization coefficient, $\alpha_\nu^{\mathrm{abs}}$ the thermal absorption opacity and $B_\nu(T)$ is the Planck function. To solve the transfer problem for isotropic scattering and thermal emission, equation (12) needs to be solved for S_ν. Since this is an implicit function of S_ν, the Lambda Iteration procedure iteratively applies the Lambda Operator and computes the new S_ν until convergence is reached. A faster variant of this procedure is the Accelerated Lambda Iteration procedure (ALI), which uses an approximate operator Λ^*.

2.3.1. Accelerated Lambda Iteration

As mentioned before, the RTE is solved by linearizing the equation using a Lambda operator. In a gridded source model (in this case the temperature grid), the Λ-operator is merely a matrix describing how the radiation field in each cell i depends on all the other cells. This way the equation can be solved using matrix operations, which can easier be computed than the integrals and differentials in the formal RTE. There is, however, still a complication. Since S_ν is determined by the temperature, which is again related to the mean intensity, equation (11) becomes implicit:

$$J_\nu = \Lambda \left[S_\nu(T)\right] = \Lambda \left[S_\nu(J_\nu)\right] \ . \tag{13}$$

Calculating this would require matrix inversion, which can computationally be very expensive. This problem can be avoided by using a iterative scheme, where an updated

---

[4] For more information on RADICAL, its availability and related publications see http://www.mpia-hd.mpg.de/homes/dullemon/radtrans/radical/

[5] A similar Short Characteristics method in spherical coordinates is discussed in Busche & Hillier (2000).

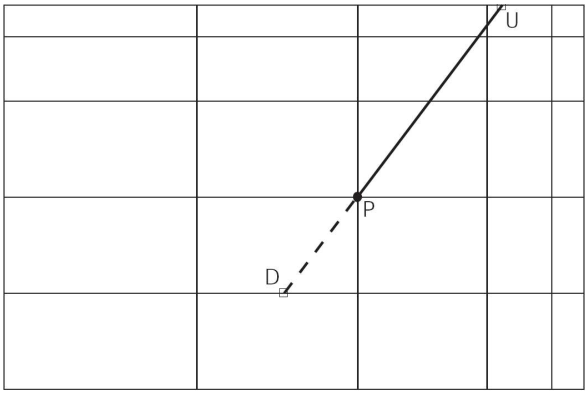

Fig. 3. An illustration of the Long Characteristics (LC) method in Cartesian coordinates. The intensity at point P is computed by integrating the transfer equation along the entire ray from the upstream boundary (point U) towards point P. This figure was obtained from Dullemond & Turolla (2000).

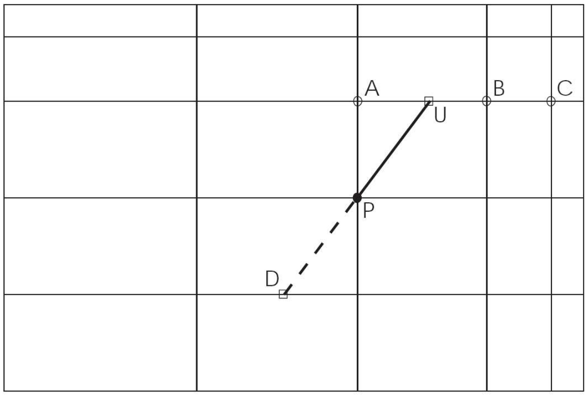

Fig. 4. An illustration of the Short Characteristics (SC) method in Cartesian coordinates. The short characteristic is the line connecting point U to D through P. The value of the intensity at U is determined by quadratic interpolation between the points A, B and C. This figure was obtained from Dullemond & Turolla (2000).

value of J_ν is obtained by having Λ operate on the previous source function, $S^\dagger_\nu(J_\nu)$,

$$J_\nu = \Lambda \left[S^\dagger_\nu(J_\nu)\right] \ . \tag{14}$$

This function is iterated until the solution converges. Since $S^\dagger_\nu(J_\nu)$ is already known, this only involves matrix multiplication, which is generally much faster than matrix inversion. Although this methods is already much faster, yet another problem can occur. Since the final solution is not known, the iteration is checked using the difference between two subsequent solutions. This relies on the assumption that the convergence goes fast and that the corrections in each step are large. However at large optical depths this is not the case, the radiation will quickly loose all “memory” of its origin and will tend to the local source function. The distance over which the information travels is about one mean free path, so the number of iterations scales as $\propto \tau^2$ (Hogerheijde & van der Tak, 2000). This effect makes it hard to determine whether the iteration has converged.

Accelerated or Approximated Lambda Iteration (Rybicki & Hummer, 1991), circumvents this problem by defining an approximate operator Λ^* such that

$$J_\nu = (\Lambda - \Lambda^*)[S^\dagger_\nu(J_\nu)] + \Lambda^*[S_\nu(J_\nu)] \ . \tag{15}$$

Since this operation again does require matrix inversion, Λ^* must be chosen such that it can easily be inverted, but also converges fast. That is, J_ν must be dominated by the second term on the right hand side of the equation, where Λ^* works on the *current* source function as opposed to the solution from the previous iteration.

A good choice for Λ^* is found to be the diagonal, or sometimes tri-diagonal, part of the full operator Λ (Olson et al., 1986). This way Λ^* describes the radiation field generated in the cell itself and, in case of the tri-diagonal matrix, the surrounding cells. Equation (15) then gives J_ν as the sum of the field generated by each cell, due to the previous solution of the source function $((\Lambda - \Lambda^*)[S^\dagger_\nu])$, and a solution of the local radiation field $(\Lambda^*[S_\nu])$. In optically thick cells, the radiation field is close to the local source function and so equation (15) converges much faster than equation (14). For optically thin cells, both methods converge equally fast (Hogerheijde & van der Tak, 2000).

2.3.2. Short Characteristics

In order to carry out the (Accelerated) Lambda Iteration procedure, a numerical implementation of the Lambda Operator Λ is needed. In Cartesian coordinates, the formal transfer equation (eq. (8)) becomes

$$\frac{\mathrm{d}I_\nu}{\mathrm{d}s} \equiv \omega_x \frac{\partial I_\nu}{\partial x} + \omega_y \frac{\partial I_\nu}{\partial y} = \alpha_\nu (S_\nu - I_\nu) \ , \tag{16}$$

where translational symmetry in the z-direction was assumed.

To carry out the numerical implementation of the Lambda Operator, equation (16) must be integrated for given S_ν and α_ν. This is done on a 2-dimensional spatial grid $\mathbf{x} = (x_i, y_j)$, for a given set of directions $\omega = \{\omega_k\}$ and frequencies $\nu = \{\nu_l\}$. This gives the specific intensity $I(x_i, y_j; \omega_k, \nu_l)$ for all i, j, k, l. For a given point $P = (x_i, y_j)$ and on a single direction and frequency, $\omega = \omega_k,\ \nu = \nu_l$, the integration of equation (16) can numerically solved along the entire ray (or characteristic) starting at the upstream boundary, heading “downstream” (i.e. the direction where the radiation comes from) and ending at point P (see figure 3). This direct integration along the entire ray is called the Long Characteristics (LC) method. This method is accurate and reliable, but it is very time consuming due to computational redundancy. For instance, if a spatial grid of size $N \times N$, a set of N_ω directions and of N_ν frequencies are used, the LC method typically takes in the order of N integration steps. This means that the total computing time scales as

$$t_{\mathrm{CPU}} \propto N^3 \times N_\omega \times N_\nu \ . \tag{17}$$

The so-called Short Characteristics method (SC; see figure 4) is a method which does not have this redundancy. Instead of integrating along the entire ray, the integration is only is only performed along the piece of the ray which connects a point U on the grid upstream of P to the closest intersection downstream of P (D). The intensity at P is then given by

$$\begin{aligned} I_\nu(P;\omega) \; &= \; e^{-\tau_\nu} I_\nu(U;\omega) + \\ & \int_0^{\tau_\nu} e^{-\tau'_\nu} S_\nu(\mathbf{x}(\tau'_\nu);\omega) \mathrm{d}\tau'_\nu \; , \end{aligned} \tag{18}$$

where τ_ν is the optical depth between points U and P. The upstream intensity $I_\nu(U;\omega)$ is interpolated using the intensities at the points A, B and C.

The integral along the upstream part of the ray (i.e. between U and P) can be computed by interpolating the source function $S_\nu(\mathbf{x}(\tau'_\nu);\omega)$ between the points D, P and U. For this interpolation Olson & Kunasz (1987) obtain:

$$\begin{aligned} I_\nu(P;\omega) \; &= e^{-\tau_{\nu,U}} I_\nu(U;\omega) \; + \; u_\nu S_\nu(U;\omega) + \\ & p_\nu S_\nu(P;\omega) \quad + \; d_\nu S_\nu(D;\omega) \; , \end{aligned} \tag{19}$$

with

$$u_\nu = e_0 + \frac{e_2 - (2\tau_{\nu,U} + \tau_{\nu,D})e_1}{\tau_{\nu,U}(\tau_{\nu,U} + \tau_{\nu,D})} \tag{20}$$

$$p_\nu = \frac{(\tau_{\nu,U} + \tau_{\nu,D})e_1 - e_2}{\tau_{\nu,U}\tau_{\nu,D}} \tag{21}$$

$$d_\nu = \frac{e_2 - \tau_{\nu,U} e_1}{\tau_{\nu,D}(\tau_{\nu,U} + \tau_{\nu,D})} \tag{22}$$

$$e_0 = 1 - e^{-\tau_{\nu,U}} \tag{23}$$

$$e_1 = \tau_{\nu,U} - e_0 \tag{24}$$

$$e_2 = \tau^2_{\nu,U} - 2e_1 \tag{25}$$

where $\tau_{\nu,U}$ and $\tau_{\nu,D}$ are the depths at U and D respectively.

By integrating over all short characteristics, a good approximate solution of the transfer equation can be obtained. The order of this integration is crucial, since the upstream intensities $I_\nu(A;\omega)$, $I_\nu(B;\omega)$ and $I_\nu(C;\omega)$ have to be known before equation (19) can be evaluated. In order to do so, the grid must be swept from the two upstream boundaries towards the two downstream boundaries.

Since the path over which the integral in performed is much shorter, the Short Characteristics method is much faster than the Long Characteristic method. For the same setup as described earlier, the computational time scales as

$$t_{\mathrm{CPU}} \propto N^2 \times N_\omega \times N_\nu \; , \tag{26}$$

which is a factor N shorter than in the case of LCs (Dullemond & Turolla, 2000).

In order to use this SC method on axisymmetric grids it needs to be transformed to spherical coordinates. This introduces additional problems which need to be solved. Therefore, two sets of coordinates are introduced. First, a spherical coordinate system (R, Θ, Φ) where Θ is the latitude and Φ the azimuth. Axial symmetry is assumed, so any dependence on Φ is suppressed. Radiation, however, is still allowed to travel along the $\partial/\partial\Phi$ direction. To describe the local radiation field at each point $P = (R, \Theta)$, a second coordinate system needs to be introduced, consisting of two independent angles on the "sky" of $P = (R, \Theta)$: θ and ϕ. The local sky is chosen such that the north pole coincides with the outward pointing radial direction. The θ angle is the angle with respect to that north pole. The ϕ angle is chosen in such a way that $\phi = 0$ points parallel to the equator of the global coordinate system (see figure 5 for more information). As in most transfer theory equations, $\mu \equiv \cos\theta$ is used instead of θ. Using these coordinates, the specific intensity depends on the two spatial coordinates R and Θ, the direction of the ray μ, ϕ and the frequency ν, or

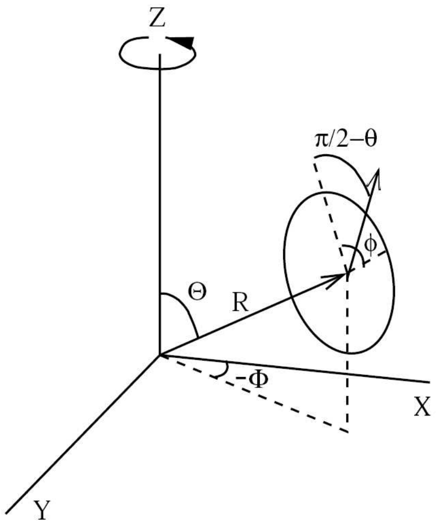

Fig. 5. The global (R, Θ, Φ) and local (θ, ϕ) coordinate systems used to describe the radiation field. Here $\pi/2 - \theta$ is shown instead of Θ for clarity of illustration. This figure was obtained from Dullemond & Turolla (2000).

$$I = I_\nu(R, \Theta; \mu, \phi) \tag{27}$$

The transfer equation (equation (8)) in these coordinates reads:

$$\begin{aligned} \frac{\mathrm{d}I_\nu}{\mathrm{d}s} \; &\equiv \; \mu\frac{\partial I_\nu}{\partial R} - \frac{\sqrt{1-\mu^2}}{R}\sin\phi\frac{\partial I_\nu}{\partial \Theta} + \frac{1-\mu^2}{R}\frac{\partial I_\nu}{\partial \mu} \\ & - \frac{\cos\phi}{\tan\Theta}\frac{\sqrt{1-\mu^2}}{R}\frac{\partial I_\nu}{\partial \phi} \\ & = \; \alpha_\nu(S_\nu - I_\nu) \; . \end{aligned} \tag{28}$$

While solving the problem of long computational times for 3D geometries, the use of spherical coordinates has the disadvantage that, contrary to what happens for Cartesian coordinates, the photon angles μ and ϕ are no longer con-

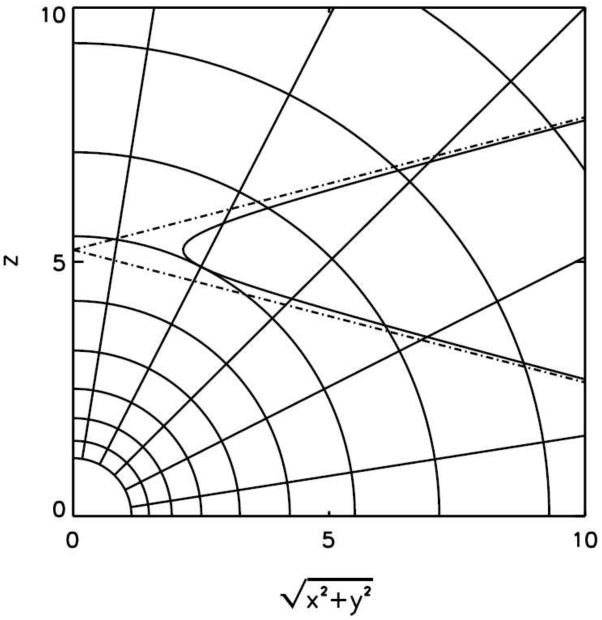

Fig. 6. An example of the projection of a Long Characteristic (LC) in the space spanned by $\sqrt{x^2+y^2}$ ($=R\cos\Theta$) and Z. Only the upper right quadrant is shown. The vertical axis is the symmetry axis and the horizontal axis the equator. The dot-dashed lines represent the asymptotes of the hyperbolic characteristic. This figure was obtained from Dullemond & Turolla (2000).

stant along the rays. The variations of R, Θ, μ and ϕ along the path are

$$\frac{\mathrm{d}R}{\mathrm{d}s} = \mu \, , \qquad \frac{\mathrm{d}\Theta}{\mathrm{d}s} = -\frac{\sqrt{1-\mu^2}}{R}\sin\phi \, , \tag{29}$$

$$\frac{\mathrm{d}\mu}{\mathrm{d}s} = \frac{1-\mu^2}{R} \, , \qquad \frac{\mathrm{d}\phi}{\mathrm{d}s} = -\frac{\sqrt{1-\mu^2}}{R}\frac{\cos\phi}{\tan\Theta} \, , \tag{30}$$

where s is the path length. From this the four relevant coordinates can be derived:

$$R^2 = b^2 + s^2 \, , \tag{31}$$

$$\cos\Theta = \frac{z_0 + s\cos\Theta_\infty}{\sqrt{b^2+s^2}} \, , \tag{32}$$

$$\mu = \frac{s}{\sqrt{b^2+s^2}} \tag{33}$$

$$\text{and} \tag{34}$$

$$\sin\phi = \frac{b^2\cos\Theta_\infty - z_0 s}{b\sqrt{b^2+s^2-(z_0+s\cos\Theta_\infty)^2}} \, , \tag{35}$$

where b is the impact parameter of the ray with respect to the origin, z_0 is the height above the mid-plane of closest approach to the symmetry-axis and Θ_∞ the inclination at infinity. These variations cause the straight ray to become warped. In the space spanned by $R\cos\Theta$ and Z it becomes a hyperbola, due to the projection effects caused by eliminating the Φ dependence. This is illustrated in figure 6.

The only interesting characteristics for numerical implementation are those that pass through a grid point $P = (R_k, \Theta_l)$ and are tangent to one of the local discrete ordinates (μ_i, ϕ_j) are interesting. Once $R_k, \Theta_l, \mu_i, \phi_j$ are fixed, such a characteristic is unique and the values of its parameters are

$$b^2 = R_k^2(1-\mu_i^2) \, , \tag{36}$$

$$\cos\Theta_\infty = \mu_i\cos\Theta_l + \sqrt{1-\mu_i^2}\sin\Theta_l\sin\phi_j \, , \tag{37}$$

$$z_0 = R_k\Big[(1-\mu_i^2)\cos\Theta_l - \mu_i\sqrt{1-\mu_i^2}\sin\Theta_l\sin\phi_j\Big] \, . \tag{38}$$

The short characteristic is then defined as the section of the curve that starts at the closest intersection with the grid *upstream* of $P = (R_k, \Theta_l; \mu_i, \phi_j)$ (point U), passes through P and ends at the closest intersection with the grid *downstream* of P (point D). The locations of the points U and D are therefore defined as the values of parameter s along the ray, s_U and s_D, which can be found by solving equations (31) and (32) with $R = R_K$ and $\Theta = \Theta_L$, where $K = k-1,\ k,\ k+1$ and $L = l-1,\ l,\ l+1$. Both $R = R_k$ and $\Theta = \Theta_l$ need to be included because the characteristic may intersect the same Θ or R grid line twice. In principle, each equation has two solutions for a given value of K and L, yielding 12 possible roots

$$s_{1\ldots6} = \pm\sqrt{R_K^2 - b^2} \, , \tag{39}$$

$$s_{7\ldots12} = \frac{1}{\cos^2\Theta_\infty - \cos^2\Theta_L}\Big\{ -z_0\cos\Theta_\infty \pm \cos\Theta_L\sqrt{b^2\left(\cos^2\Theta_\infty - \cos^2\Theta_L\right) + z_0^2}\Big\} \, . \tag{40}$$

Two of these solutions give $s = s_P$, i.e. $P = (R_k, \Theta_l)$ itself, and are of no interest. Of the remaining 10 roots, some are complex and can be rejected. The points D and U are selected by demanding that $s > s_P$ (or $s < s_P$, for U) and that $|s - s_P|$ is a minimum.

Although, as shown, SCs can be defined in spherical coordinates, there are two problems, which need to be solved before they are useful for a transfer algorithm. The first problem, which was mentioned earlier, is the fact that μ and ϕ change along the ray. Therefore, not only the spatial coordinates need to be interpolated, but μ and ϕ as well in order to evaluate $I_\nu(U,\omega)$. This is because the intensities at points A, B and C are known only for a discrete set of directions which are in general different from the values of μ and ϕ in U.

The second and more challenging problem is that in spherical coordinates the upstream and downstream boundaries are not well defined. Radial infinity is both the up- and downstream direction, while in Θ there is no clear boundary at all. If the grid is evaluated (or swept) simply from $\Theta = 0$ to $\Theta = \pi$, there is a possibility that the intensity in A, B or C is not known before the evaluation of the transfer integral along the short characteristic (eq. (18)) is performed. Such a situation is sketched in figure 7. The interpolation of the intensity in U makes use of the points A, B and C, but since A coincides with P, the intensity at the point $A \equiv P$, has not been computed yet.

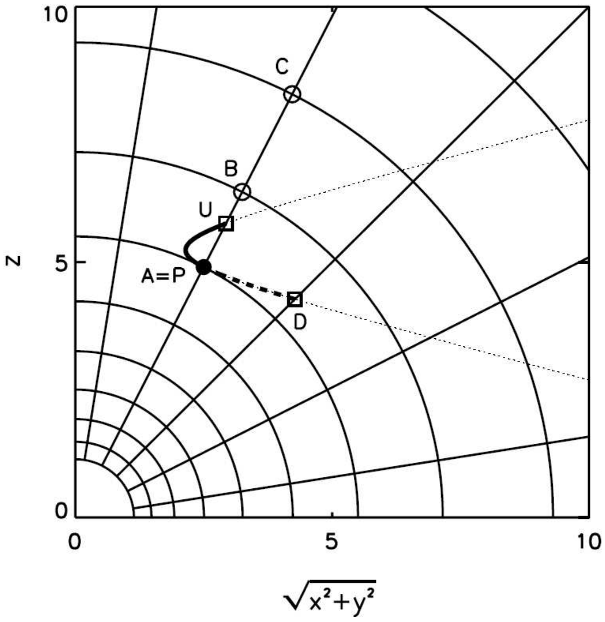

Fig. 7. An example of a Short Characteristic (SC) in spherical coordinates (the heavy line connecting U to D through P). As in figure 4 the downstream part of the SC is dashed. The dotted line shows the complete ray to which the SC belongs. This figure was obtained from Dullemond & Turolla (2000).

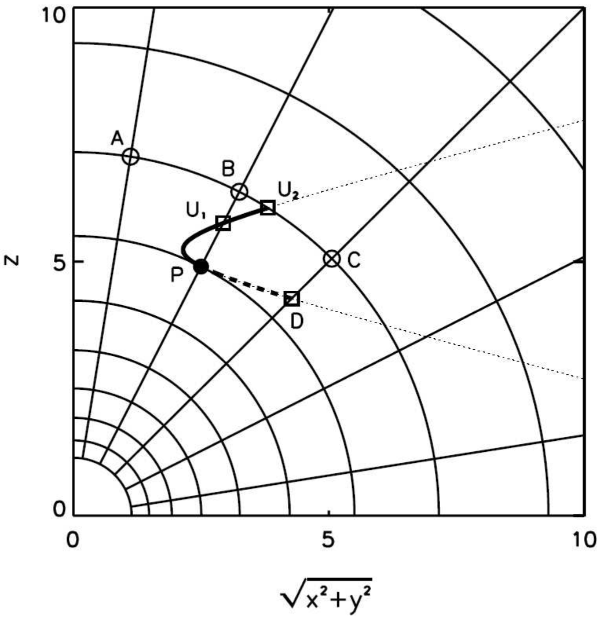

Fig. 8. An example of an Extended Short Characteristic (the heavy line connecting U_2 to D through P) in spherical coordinates. It is the extended version of the SC shown in figure 7. The ESC does not have the same problems as the SC because for the ESC none of the points A, B or C coincides with point P. This figure was obtained from Dullemond & Turolla (2000).

2.3.3. Extended Short Characteristics

The problem of unknown intensities can be solved by modifying the definition of short characteristics to be the part of the ray that connects P, not with just the nearest grid line intersection, but with the nearest $R = R_k$ grid line intersection, i.e. the nearest radial shell (Dullemond & Turolla, 2000). Such an "extended short characteristic" (ESC) is illustrated in figure 8. For an ESC, the point U may be located on the $R = R_{k-1}$, or the $R = R_{k+1}$ shell, or back at $R = R_k$. This means that between P and U, more than one Θ grid line may be crossed. In figure 8 these crossings are denoted with U_1 and U_2[6]. The downstream point D remains the same as for SCs.

When a proper sweeping scheme is chosen (see next section), the problem of unknown intensities only occurs when rays end up at the same Θ grid line as where they started (as illustrated in figure 7). By extending only these SCs and leaving the rest short, the problem is avoided and the calculation time remains as minimal as possible. This method is called the Minimally Extended Short Characteristics scheme (MESC). MESC is almost as accurate as ESC, but much faster.

2.3.4. The sweeping scheme

As mentioned above, using the MESC scheme, the grid can be swept systematically without encountering unknown intensities. The process starts at the outer boundary and integrates inward only those ESCs for which $\mu_i \leq 0$ (i.e. inward pointing, so that the upstream intensity is known). The sweeping order in Θ is from $\Theta = 0$ to $\Theta = \pi$ and then back.

The intensity at each $P = (R_k, \Theta_l)$ is found for all $\mu_i \leq 0$ and ϕ_j by tracing the ESCs back to their upstream starting point U_m. The intensity at U_m is found by interpolation, just like in the SC method. The formal transfer equation is then integrated along each segment of the ESC connecting U_m to P, according to equation (19). This gives

$$I_\nu(P) = e^{-\tau_m} I_\nu(U_m) + \sum_{i=1,m} e^{-\tau_{i-1}} \times \\ (u_{\nu,i} S_{\nu,i} + p_{\nu,i-1} S_{\nu,i-1} + d_{\nu,i-2} S_{\nu,i-2}) \;, \quad (41)$$

where τ_i is the optical depth from P to U_i and the index i denotes the quantity evaluated at U_i (e.g. $S_i \equiv S(U_i)$; $i = 0$ refers to P and $i = -1$ to D). The u's, p's and d's are defined as in equations (20), (21) and (22), but with $\tau_{\nu,U}$ replaced by $(\tau_{\nu,i} - \tau_{\nu,i-1})$ and $\tau_{\nu,D}$ by $(\tau_{\nu,i-1} - \tau_{\nu,i-2})$.

The integration is then repeated moving towards smaller radii, until the inner boundary is reached. Here the contribution of the central source is included.

Then the integration goes back towards larger radii, until the outer edge is reached. By then the radiation field on the grid $I_\nu(R_k, \Theta_l; \mu_i, \phi_j)$ is known (Dullemond & Turolla, 2000).

---

[6] In the rest of the paper the single downstream intersection with a grid line will be denoted with D (or U_{-1}), and the intersections upstream of P with $U_i (i = 1, \ldots, m)$. Therefore, the point U_m is the starting point of the ESC (equivalent to the point U for SCs), where the intensity must be found by interpolation.

Table 1. This table lists the parameters used for the simulations. Each parameter is deviated from the default twice: a higher and a lower value. The only exception to this is the closing angle η, for which both deviations are higher than the default. Also one simulation was made using continuous star formation with a given SFR. All simulations were calculated for inclinations 0, 30, 60 and 90 degrees. The names chosen for the simulations represent the deviations.

name	$\log M_{\rm SB}$ [log $M_\odot$]	α [$M^{-\alpha}$]	τ	η [$0-1$]	δ [°]
DEFAULT	9	2.35	10	0.3	$0, 30, 60, 90$
LOWMASS	8	2.35	10	0.3	$0, 30, 60, 90$
HIGHMASS	10	2.35	10	0.3	$0, 30, 60, 90$
LOWALPHA	9	1.3	10	0.3	$0, 30, 60, 90$
HIGHALPHA	9	3.3	10	0.3	$0, 30, 60, 90$
LOWTAU	9	2.35	1	0.3	$0, 30, 60, 90$
HIGHTAU	9	2.35	100	0.3	$0, 30, 60, 90$
COVERED1	9	2.35	10	0.5	$0, 30, 60, 90$
COVERED2	9	2.35	10	0.7	$0, 30, 60, 90$
CONTINUOUS†	100$M_\odot$/yr	2.35	10	0.3	$0, 30, 60, 90$

† : In this simulation the stars were not formed in one instantaneous burst, but continuously with a SFR of 100 $M_\odot$/yr. After 10 Myr this results in the formation of 1×10^9 $M_\odot$ of stars.

2.4. Spectra

Once the radiation field is known, spectra can be produced. First an image is created by integrating the source function along characteristics through the medium (ray tracing). Each ray represents one pixel of the image. Spectra can be derived by making images at a range of frequencies, and integrating these over an artificial detector aperture.

Resolution problems may occur, since the source spans a large range in R. The central parts of the image are often much brighter than the rest, but cover a much smaller fraction of the image. The spectrum may therefore contain significant contributions of flux from both the central parts and the outer regions of the image. Unless the image resolve all spatial scales of the object, the spectra produced in such a way are unreliable.

Therefore, rather than arranging the pixels over a rectangle, as in usual images, they are arranged in concentric rings. The radii of these rings are related to the radial grid points of the transfer calculation; one ring for each R_i. To resolve the central source, some extra rings need to be added. In RADICAL 5 extra rings are added, so that the number of rings (N_b) is $N_R + 5$. The number of pixels in each ring is slightly less straightforward to choose, but for reliable spectra it is generally sufficient to take $2N_\Theta$, where N_Θ is the number of Θ grid points, counted from pole to pole. Using these kind of images, all relevant scales are resolved, while using only a fairly limited number of pixels (Dullemond & Turolla, 2000).

Table 2. This table lists the parameters which determine the simulations, but were not varied. The upper part of the table lists the SB99 parameters, the lower part the RADMC parameters.

name	value	
IMF upper mass limit	100	$M\odot$
IMF lower mass limit	1	$M\odot$
supernova cut−off mass	8	$M\odot$
black hole cut−off mass	120	$M\odot$
initial time	0.01	Myr†
time step	0.1	Myr
end time	20	Myr
wind model	theoretical‡	
atmosphere model	Pauldrach/Hillier‡	
metallicity of uv line spectrum	solar	
r_0	100	pc
dr_0	50	pc

† : Due to numerical reasons SB99 can not start the simulation at t=0.

‡ : see Leitherer et al. (1992) and Leitherer et al. (1999) for more information.

3. The simulations

In this section, the simulation setup and the parameter space are discussed. As shown in figure 1, there are 6 parameters, which control the simulation: the combined mass of the stars in the starburst $M_{\rm SB}$, the star formation rate (SFR), the IMF slope α, the closing angle of the torus η, the dust density expressed in the face-on V-band optical depth τ and the observation declination δ.

This parameter space has been explored, starting with values chosen either from literature or at random. In order to verify the results of the simulations, a reference data set was made using IRAS data of starburst galaxies taken from the extended 12 micron galaxy sample (Rush et al., 1993) and the IRAS Bright Galaxy Sample (Condon et al., 1991).

From these simulations a default set is chosen, which fits the data best. This set will be referred to as DEFAULT. This set was chosen as starting point for a more systematic sweep of the parameter space. Each parameter was both increased and decreased with respect to the default value. Exceptions are the closing angle η, the inclination δ and the SFR. Both permutations of η are higher than the default value. The inclination was varied in all simulations: each setup was calculated for δ = 0, 30, 60 and 90 degrees. The SFR was only used in one simulation. In the other simulations, all stars are formed instantaneous. The entire parameter space is listed in table 1.

3.1. STARBURST parameters

The starburst in the center of the simulation has a vast amount of parameters. Only three are chosen as variables, in order to reduce the amount of data and to avoid unnec-

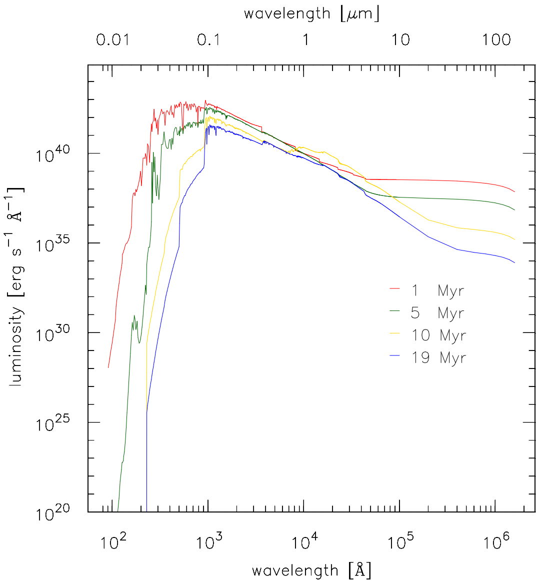

Fig. 9. An example of the output spectra of SB99. These results were taken from the default simulation. As can be seen, the spectra cover a large frequency range; from the UV up to 100μm in the IR regime. For more information about the used parameters, see tables 1 and 2.

essary redundancy. Also these parameters are expected to have the largest influence on the final results. The fixed parameters are listed in table 2.

The variable parameters are the total mass of the stars involved in the starburst ($M_{\rm SB}$), the star formation rate (SFR) and the IMF slope[7] (α). These were chosen, because the large luminosities of ULIRGs could be explained by a high total burst mass, a high SFR or by a lower IMF slope exponent. Adding more stars or increasing the SFR will scale the entire spectrum, whereas decreasing the IMF slope increases the relative number of heavy stars, leading to more UV radiation and therefore more heating flux (as suggested in Heckman, 1998).

With all these parameters set the starburst simulation can be run. This produces spectra which cover a large wavelength range. A few examples of these spectra are shown in figure 9. Since the dust code RADMC has a limitation on the amount of channels the input spectrum can have, the output spectra of SB99 need to be re-binned. A second limitation of the radiative transfer codes is that their output spectra have the same frequency points as the input spectra. Therefore the re-binning of the SB99 output is performed in such a way that both the UV/optical part of the spectra (which provides the energy for the dust heating) and the IR regime (which is the part of the spectrum of interest) are covered well. This is achieved by binning the UV/optical part of the spectrum and adding the 10, 20, 60 and 100 μm points. These four bands are used to compare the simulation results to the four IRAS bands.

3.2. Dust setup

The dust distribution is made by creating a polar grid, with a density on each grid point. The toroidal shape was created by introducing a Gaussian distribution in both the r- and θ-direction:

$$\rho\left(r,\theta\right) = \exp\left[-\frac{1}{2}\left(\frac{\pi/2-\theta}{\eta}\right)^2 - \frac{1}{2}\left(\frac{r-r_0}{dr_0}\right)^2\right] , \qquad (42)$$

where $\rho\left(r,\theta\right)$ is the dust density on each grid point, r is the radial direction, θ the angular direction, r_0 the radius of the torus, dr_0 radial scale size the and η the closing angle. This density distribution is then scaled by scaling the edge-on optical depth (obtained by integration along the line of sight) to the desired optical depth τ. Two examples of resulting density distribution are plotted in figure 10. From this two dimensional grid, a three dimensional grid is made by first mirroring the grid in the r-axis and then rotating this semi-circle around the z-axis.

In the dust setup a number of parameters were fixed as well. These are the radius r and the radial scale size dr. These were fixed mainly to reduce the number of simulations, but as well because the influence of these parameters is expected to be limited to scaling of the results because the radiating area of the torus changes. The closing angle η, for which a similar argument can be used, was changed to investigate it's influence on the inclination depenency of the results.

3.3. Infrared output

In this subsection, the IR output of the simulation is discussed, using DEFAULT as example. As mentioned before, the code produces four fluxes as a function of time. These fluxes are used to calculate the IR luminosity (L_{IR}) using the definitions given in Sanders & Mirabel (1996) and Kim & Sanders (1998):

$$\begin{aligned} F_{IR} \;=\; & 1.8\times10^{-14}\,(13.48f_{12}+5.16f_{25}+ \\ & 2.58f_{60}+f_{100}) \end{aligned} \qquad (43)$$

and

$$L_{IR} = 4\pi D^2 F_{IR} \ , \qquad (44)$$

where F_{IR} is the total IR flux in units of Wm^{-2}, f_n are the four IRAS fluxes in units of Jy and D the distance in meters. The distances of the reference data sets were calculated using their observed redshift:

$$D_{\rm Mpc} = \frac{cz}{H_0}\left(1+\frac{z(1-q_0)}{\sqrt{1+2q_0z}+1+q_0z}\right) , \qquad (45)$$

with the deceleration parameter q_0 defined as:

$$q_0 = \frac{\Omega_m}{2} - \Omega_\Lambda \ . \qquad (46)$$

In these equations c is the speed of light, z the redshift, H_0 the Hubble parameter (72 km s^{-1} Mpc^{-1} was used), Ω_m

---

[7] The IMF is defined as: $\Psi(M) \propto M^{-\alpha}$.

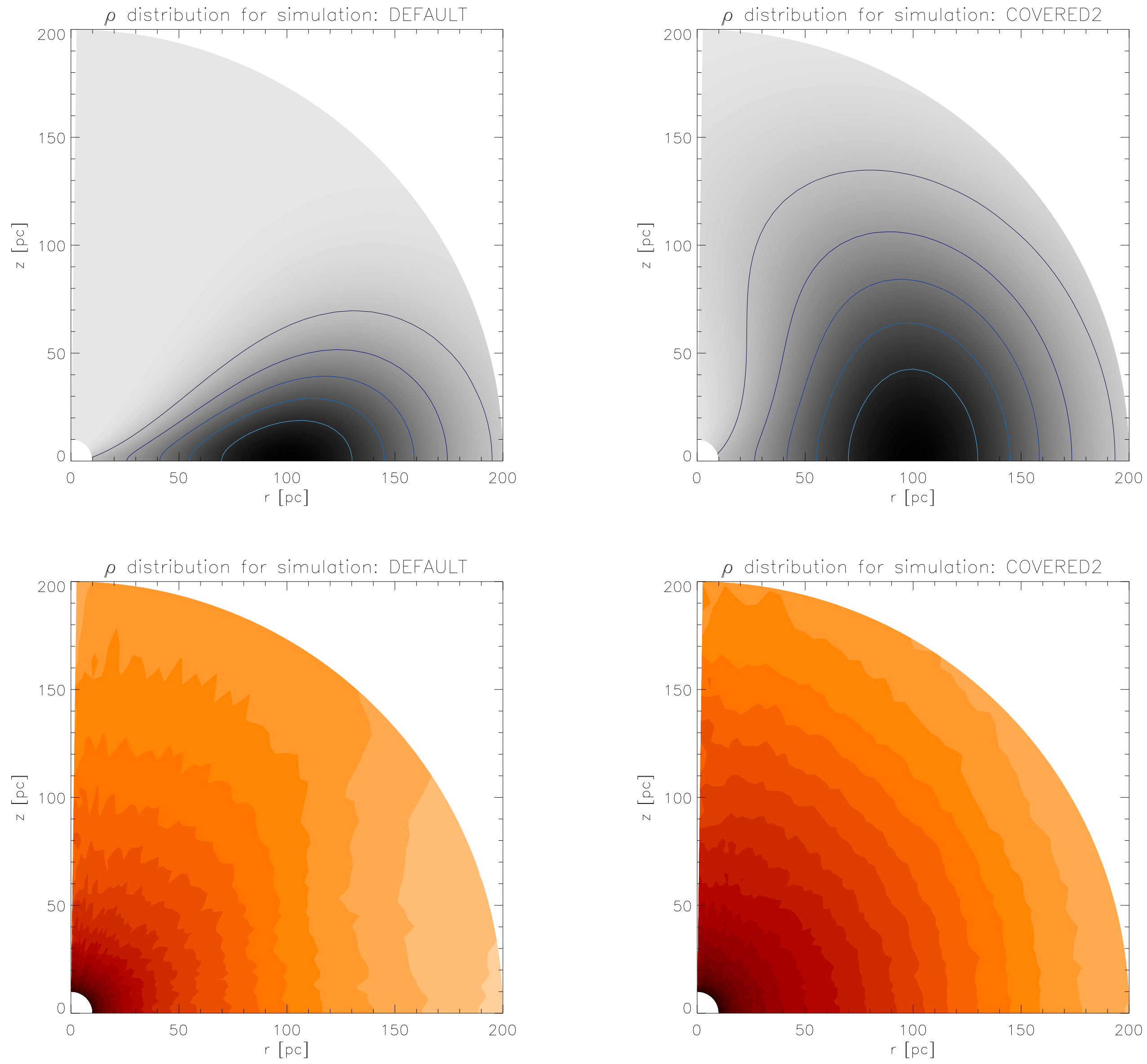

Fig. 10. These figures show two examples of the dust and temperature distributions resulting from the simulations. The top panels show the dust density in gray scale, where dark colors indicate regions with high densities and light colors are low density regions. Also some blue contours are added to enhance the shape of the density profile. The bottom panels show the temperature distribution. In these panels, dark colors indicate high temperatures (maximum contour at 270K) and light colors cooler regions (lowest contour drawn at 30K). The number of levels in these plots was decreased to make the difference between the two plots stand out more. The left panels show the default simulation and the right ones a setup with $\eta = 0.7$.

the matter density (0.27) and Ω_Λ the dark energy density (0.73) (Peacock, 1999; Bennett et al., 2003).

The results are plotted in figure A.1. The first 4 panels show the results of the IR fluxes. As can be seen the simulation results match the reference set quite well. Only the shortest wave length seems to be a poor fit. This is probably due to the fact that the dust is simulated using only one dust species, which was assumed to be gray, i.e., radiation of all frequencies is fully absorbed by all grains and re-radiated using a black body profile. This affects the short wavelength radiation since that is mostly emitted by very small grains, which physically do not behave like black bodies. For these grains effects like quantum heating, PAHs and silicate features play an important role.

The calculated L_{IR} also covers the desired range. At the peak of their activity the luminosity of the starburst is 10^{12} L$\odot$, which makes them ULIRGs. They remain that luminous for about 3 Myr, after which they slowly dim and reach the LIRG regime.

The color-luminosity diagrams (CLDs) in the last three panels show similar results. The 20μm$/100\mu$m and 60μm$/100\mu$m results match the data, whereas the 10μm$/100\mu$m is a poor fit to the data. This is again an indication that the cold (60μm) and warm ($20\ \mu$m) dust are modeled well, but that there seems to be a lack of radiation coming from hot dust and line features.

Another aspect which can be seen in the results is the large inclination dependency of the results. The difference between edge-on and face-on ranges from 0.5 magnitudes at 100μm up to 3 magnitudes at 10μm, with an average of 0.75 in the L_{IR}. In the last 3 panels there is also a large separation between the face-on and edge-on results at short wavelengths. This effect is caused by the dust distribution. As can be seen in figure 10, the resulting temperature distribution is not spherical. Because the dust density is larger along the edge-on axis, the temperature gradient along this axis is larger than the face-on temperature gradient. This causes the areas with lower temperature to become more flattened, compared to the inner, high temperature areas. When this temperature distribution is viewed edge-on, the cooler isothermal surfaces are seen at their maximum surface area and when observed face-on, their surface areas decrease rapidly. The inner high temperature regions are roughly spherical and will therefore look the same from all directions. This means that the overall face-on spectrum will look “hotter”, compared to the edge-on spectrum. This is also illustrated in the lower right panel of figure 10, which shows the temperature distribution of COVERED2. In this simulation, the cooler dust is nearly spherical and the inclination dependency of the 10μm flux is a magnitude lower (see figure A.9).

An interesting effect of this inclination dependency can be seen in the three CLDs in figure A.1. At short wavelengths (10μm/100μm and 20μm/100μm) the face-on observations trace the data sets, whereas the edge-on results cover an entirely different range. In figures A.8 and A.9, where the inclination effects are less, the same effect is visible. This might indicate that there is a sample of edge-on ULIRGs, which are currently either not observed, or classified as other types of galaxies.

4. Results

In this section the rest of the simulation results will be discussed. As mentioned in the previous section, each parameter was changed twice, in most cases “in both directions”. This way systematical effects can be detected. The observational inclination will not be discussed, since the effects of the inclination have already been discussed in the previous section. The figures displaying all the results of the individual simulations are put in appendix A. The figures which combine the results of the two deviations with the default simulation to show the effects the parameters have on the results are put in appendix B. A “summary” of the results is shown in figure 11.

4.1. Starburst mass

The effect of the starburst mass on the SB99 spectra is quite simple. Since this code works with a distribution of stars, integrated to a certain mass, the spectra will scale proportional to the total stellar mass. The influence on the dust is less straightforward, however. When the energy input provided by the starburst increases, the overall dust temperature will be higher and therefore, the IR spectrum will become “hotter”, i.e. the short wavelengths will increase faster relative to the long wavelengths. Also the IR luminosity is expected to increase with the stellar mass, since the energy input increases.

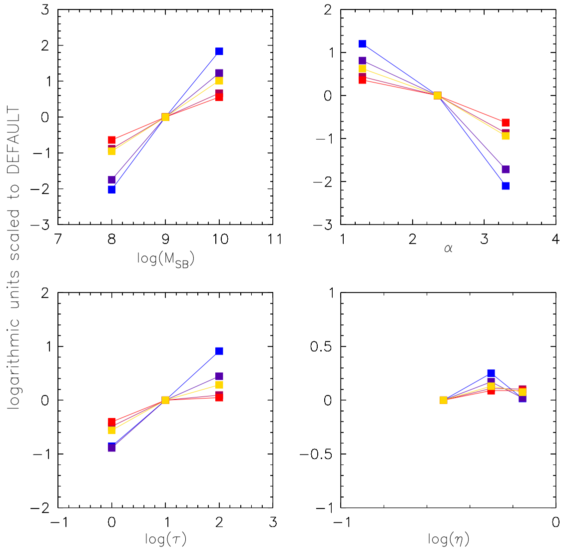

Fig. 11. These panels give a “summary” of the simulation results. The four IR fluxes (colors from blue (10μm) to red (100μm)) and the IR luminosity (yellow) are shown as a function of the various parameters (top-left: $M_{\rm SB}$, top-right: α, bottom-left: τ, bottom-right: η). The points represent the values at 2Myr, which is the time where the radiation is at its maximum. All data were scaled to the results of DEFAULT, in order to make an easy comparison. Note that the results of ρ and the SFR are not included in these plots.

The simulations confirm these expectations. Figure 11 clearly shows that the short wavelengths (blue) increase much faster than the long wavelengths (red) and that L_{IR} (yellow) increases as the mass increases.

The color-luminosity plots seem to reveal less trivial information. The first thing which can be concluded is that, assuming all the other parameters are correct, a minimal mass of 10^9M$\odot$ is needed to create enough power. Another conclusion is that, since all three simulations seem to lie on the same “track”, starburst mass and age have the same effect on the results. In other words, a young, but relatively light starburst will have the same appearance as a heavy, older starburst.

4.2. IMF slope

When the IMF slope decreases, the number of heavy stars in the starburst will increase. These high mass stars are the main source for the heating UV radiation, and so the dust temperature will increase with a shallower IMF slope. This means that varying the IMF slope would yield results similar to increasing the starburst mass.

Figure 11 shows this is indeed the case. Note that the effect seems to be reversed, but the IMF is defined as $\propto M^{-\alpha}$, so the axis is simply reversed. Interesting to see is that the effect is somewhat more complicated than for $M_{\rm SB}$. All fluxes scale proportionally to M_{SB}, in this case the effect is stronger when going from high α to the default value, then when lowering it even further. This could either be caused by the fact that for high values of α the heating process of the dust is very inefficient, or it means that there is a maximum to how much UV energy can be converted.

Figure B.2 shows that although LOWALPHA starts with higher fluxes, the values decay much faster. This is due to the short life time of the high mass stars. After about 10 Myr the low IMF case cannot be distinguished from the default case any more.

The CLDs also show this. Although the LOWALPHA tracks start at higher values of both the color and luminosity (i.e. the upper-right corner of the plot), in later stages of their evolution they coincide with the DEFAULT tracks. Therefore, the same conclusion can be drawn for the IMF slope as for the starburst mass: the data either represent young starbursts with a normal IMF, or an older population of stars with a low IMF slope.

4.3. Dust density

When changing the total amount of dust for a given energy input, there will be several effects. First, when the dust density is lower, the dust will be heated more evenly, since the radiation can travel through the dust easier. This will result in a smaller temperature gradient, and will therefore lead to a higher minimum temperature and a lower maximum temperature. The spectrum will become flatter, or "colder". Conversely high dust densities will lead to larger dust gradients and "hotter" spectra. This effect can also be seen in the results of the simulations in figure 11, which shows that the variation of τ has a similar effect as $M_{\rm SB}$ and α.

Another effect is that, due to the larger temperature gradient, the inclination dependency will increase for larger τ. In figure B.3, this effect can especially be seen in the first two panels, where the edge-on and face-on results are almost the same for LOWTAU, whereas the results for HIGHTAU differ by up to 4 magnitudes.

A third effect is the increase in the total luminosity, simply because there is more radiating dust.

All these effects can be found in the color-luminosity plots. When going from LOWTAU to DEFAULT especially L_{IR} increases, resulting in a shift to the right. But when τ increases even more, the color changes rapidly, and the track moves up-right. Again, due to the inclination effects, the edge-on results do not match the reference sets. The edge-on results of LOWTAU are better, because they suffer less from inclination effects, however, they are worse fits than the face-on DEFAULT results.

Like in the previous simulations, there is a degeneracy between τ and time. Young populations surrounded by moderate density dust have the same IR properties as older, more enshrouded starbursts.

4.4. Closing angle

The effect of the closing angle is not as profound as that of the other parameters. The only major effect it seems to have is that the inclination dependency effects are reduced. This is caused by the fact that the density gradient in the θ direction is smaller (also see figure 10). The extreme case would be a simulation with $\eta = 1$, which is a shell of dust and of course a shell has no inclination dependency at all.

Although the inclination effects are less in simulations with a higher closing angle, the edge-on tracks in the color-luminosity tracks (figures A.8, A.9 and B.4) still do not fit the reference data.

The shape of the spectrum also changes when the closing angle changes, but this is due to the fact that the total amount of dust changes, because the edge-on optical depth is kept constant.

4.5. Star formation rate

So far, all simulations were made with the assumption that the stars were formed instantaneously, or, in other words, on a timescale much shorter than the evolution timescale of the stars ($\lesssim$ 1 Myr). This is based on the assumption that there is a rapid build-up of gas in the starburst environment, which at some point becomes critically dense and "ignites". It also assumes that the stellar winds and supernovae do not provide strong feedback, so that all gas can be converted into stars on a short time scale. However, the assumption that the starburst environment is less violent and more like normal star formation regions, with a steady inflow of gas, is equally valid and must be explored as well. Therefore, a starburst with continuous star formation was also simulated. The SFR was chosen to be 100 $M\odot$ yr^{-1}, which leads to the formation of 10^9 $M\odot$ of stars after 10Myr, making it comparable to the other simulations.

The results of this simulation are shown in figure A.10 and compared to DEFAULT in figure B.5. These figures show some remarkable differences between the two situations. Whereas the instantaneous burst starts at a maximum and decays rapidly after about 3 Myr, the continuous case starts at much lower values and takes quite some time to rise. After about 5 Myr the two scenarios cross and the continuous case starts to dominate. After 10 Myr it reaches its maximum, but it does not decay, since stars keep forming at a constant rate. So far the differences can be explained by the star formation history, however one difference cannot be explained by the SFR alone. Since the instantaneous burst has a SFR of 1000 $M\odot$ yr^{-1} or more, one would expect that the peak fluxes will be at least a factor of 10 higher than the fluxes of the continuous star formation. They are, however, less then a quarter of a magnitude higher. Apparently the heating of the dust is far less efficient at higher input fluxes than at moderate ones. The result is that in the CLDs both simulations are on the same track.

The significant difference between the continuous and the instantaneous star formation is that objects with instantaneous star formation are only luminous enough in the first 5 to 10 Myr, which decreases their detection rate. The continuous starbursts remain luminous as long as there is inflow of gas to feed the star formation.

5. Conclusions

Several conclusions can be drawn from the results as were presented in the previous section. The main conclusion is that our model is able to reproduce the global IR properties of starburst galaxies. All simulations cover the same evolutionary track in the color-luminosity diagrams, indicating that the macro physics are modeled well.

Not all parameters were found to have a profound effect on the results. The parameters controlling the star formation, the total stellar mass $M_{\rm SB}$ and the IMF slope α, have a large effect on the final results, whereas the influence of the dust geometry (τ and η) on the final IR properties is far less:

- $M_{\rm SB}$: Increasing the stellar mass has two effects: the spectrum becomes "hotter" and L_{IR} increases. These changes are profound: the IR fluxes change 0.6 (100μm) to 2 (10μm) magnitudes and L_{IR} changes about 1 magnitude when varying the mass.
- α: The effects of varying the IMF slope are similar to that of the stellar mass, and are less profound when decreasing α than when increasing it. Making the slope more shallow changes the fluxes 0.4 (100μm) to 1.2 (10μm) magnitudes and L_{IR} about 0.6 magnitudes. Increasing the slope changes the fluxes 0.6 (100μm) to 2.1 (10μm) magnitudes and L_{IR} about 0.9 magnitudes.
- τ: Changing the dust density has three effects. First of all the spectrum becomes hotter and the IR luminosity increases, just like when changing the star formation parameters. These effects are, however, much smaller: the fluxes only change 0-0.4 (100μm) to 0.9 (10μm) magnitudes and the total luminosity changes 0.3 to 0.5 magnitudes. A third effect is that the inclination dependency increases with increasing density. The difference in the edge-on and face-on values of L_{IR} changes from 0.2 $L_\odot$ for $\tau = 1$ to 1.2 $L_\odot$ for $\tau = 100$.
- η: Varying the closing angle only has effects on the inclination dependency of the results. The variation of L_{IR} for a "flat" torus ($\eta = 0.3$) is about 0.8 magnitudes, compared to 0.3 for a more flared torus with a closing angle of 0.7 .

Because of their large influence on the results, the star formation parameters could be determined well. It was found that the power source of starburst galaxies is a star formation region, which produces $10^9 M_\odot$ of stars (either in one instantaneous burst, or in a continuous process) with a Salpeter IMF ($\alpha = 2.35$). The influence of the dust geometry on the final IR properties was far less and therefore these parameters could not be determined to great precision. For the dust density the best fit was obtained with $\tau = 10$, but the other simulations were also reasonably well. The closing angle did not seem to have a optimum value at all. Even though the inclination effects are reduced for higher values, the edge-on results still do not match the data.

Looking at the values determined for the parameters, it seems that, although observationally starburst galaxies appear to have a very violent nature, the star formation environment is not as "exotic" as expected. The parameters of the actual star formation are the same as in "normal" star formation regions. There is no need for an adjusted IMF to increase the number of heavy stars. The only exceptional parameter needed to explain the high IR output of starburst galaxies is the high total stellar mass (or a high SFR). The dust surrounding the stars is no exception to this trend. Both the size and the V-band optical depth of the dust cloud are moderate (100 pc and 10 respectively). Also, the distribution of the dust, either a reasonably flat or a bigger, more flared torus, did not have a large influence on the final results.

A second result is the even more remarkable. In all the simulations, the data were fitted only by the face-on evolutionary tracks. All the completely edge-on results were a poor fit, or did not even cover the reference data at all. Statistically one would expect that one third of the galaxies in the sample is viewed edge-on (i.e., the observation angle with respect to the equator is lower than the closing angle η). This can have a few explanations. Either the inclination dependency resulting from our model is too large, and that extra parameters need to be added to address that problem. If this is the case, the solution is most likely found in the dust properties, since in the current set of simulations the inclination dependency is influenced most by changing the dust density. Also the assumption that the dust surrounding the star formation region has a toroidal shape can be wrong. A spherical distribution will also eliminate the inclination effects. On the other hand, if the predictions of our model are correct the implication is that there is a significant number of starburst galaxies, which are currently not detected or, more likely, not classified as such.

There are also some critical remarks that must be made about this model. Even though the general properties are explained, there are two limitations. First of all the parameter space is highly degenerate. All parameters move the evolutionary tracks more or less along the same line, which is also the direction of the evolution. The result is that the physical environment in a given starburst galaxy cannot be inferred from observations, using this model. Including other wavelength data will most likely break the degeneracy, since optical and UV data will give more information about the star forming region and millimeter observations will reveal more about the outer dust regions and the molecular environment.

A second shortcoming of the current model is that it does not explain the scatter in the reference data set well. The star formation parameters introduce no scatter; changing these parameters only shifts the tracks in the CLDs along their evolutionary tracks. Also the closing angle causes no significant scatter. The only parameter which gives rise to some scatter is the dust density. Since the scatter is not caused by the stellar environment and the large scale dust properties, the cause must lay in the small scale physics. Most likely the optical properties of the dust are the source of the scatter.

Also the 10μm fluxes as calculated by our model are a poor fit to the data. This is also due to the optical properties of the dust. In our model the dust was assumed to be gray, i.e. dust grains were expected to behave like blackbodies. However the short wave length radiation is mostly emitted by small dust grains, which physically do not behave as such. Also effects like quantum heating and features from complex grains like PAHs and silicates play an important role for these small grains.

The future of this project is clear. The model should be extended to both larger and smaller scales. On large scales it needs to be extended with a molecular environment surrounding the current dust region. Also other wavelengths need to be studied. On the other hand the small scales need to be modeled better as well. The largest shortcoming of the model is the fact that the dust is not modeled properly. In the future, effects like quantum heating and features from complex grains such as PAHs, silicates and amorphous carbon need to be included.

Acknowledgements. First of all I would like to thank Willem Baan and Marco Spaans for all their support and patience during this long project. I would also like to thank Rowin Meijerink and Kees Dullemond for their extensive support on setting up and using RADMC and RADICAL and Claus Leitherer for answering all my questions about STARBURST99. Last but not least I would like to thank all my fellow students for their input and good ideas and for test reading this paper.

References

Bennett, C. L., Halpern, M., Hinshaw, G., Jarosik, N., Kogut, A., Limon, M., Meyer, S. S., Page, L., Spergel, D. N., Tucker, G. S., Wollack, E., Wright, E. L., Barnes, C., Greason, M. R., Hill, R. S., Komatsu, E., Nolta, M. R., Odegard, N., Peiris, H. V., Verde, L., & Weiland, J. L. 2003, ApJS, 148, 1
Bjorkman, J. E. & Wood, K. 2001, ApJ, 554, 615
Blain, A. W., Smail, I., Ivison, R. J., Kneib, J.-P., & Frayer, D. T. 2002, Phys. Rep., 369, 111
Busche, J. R. & Hillier, D. J. 2000, ApJ, 531, 1071
Charlot, S. & Bruzual, A. G. 1991, ApJ, 367, 126
Condon, J. J., Huang, Z.-P., Yin, Q. F., & Thuan, T. X. 1991, ApJ, 378, 65
Downes, D. & Solomon, P. M. 1998, ApJ, 507, 615
Dullemond, C. P. & Turolla, R. 2000, A&A, 360, 1187
Genzel, R. & Cesarsky, C. J. 2000, ARA&A, 38, 761
Heckman, T. M. 1998, in Astronomical Society of the Pacific Conference Series, 127–+
Hogerheijde, M. R. & van der Tak, F. F. S. 2000, A&A, 362, 697
Kim, D.-C. & Sanders, D. B. 1998, ApJS, 119, 41
Kormendy, J. & Sanders, D. B. 1992, ApJ Lett., 390, L53
Leitherer, C. & Heckman, T. M. 1995, ApJS, 96, 9
Leitherer, C., Robert, C., & Drissen, L. 1992, ApJ, 401, 596
Leitherer, C., Schaerer, D., Goldader, J. D., Delgado, R. M. G., Robert, C., Kune, D. F., de Mello, D. F., Devost, D., & Heckman, T. M. 1999, ApJS, 123, 3
Lejeune, T., Cuisinier, F., & Buser, R. 1997, A&AS, 125, 229
Lucy, L. B. 1999, A&A, 344, 282
Meynet, G., Maeder, A., Schaller, G., Schaerer, D., & Charbonnel, C. 1994, A&AS, 103, 97
Olson, G., Auer, L., & Buchler, J. 1986, J. Quant. Spectrosc. Radiat. Transfer, 35, 431
Olson, G. & Kunasz, P. 1987, J. Quant. Spectrosc. Radiat. Transfer, 38, 325
Pascucci, I., Wolf, S., Steinacker, J., Dullemond, C. P., Henning, T., Niccolini, G., Woitke, P., & Lopez, B. 2004, A&A, 417, 793
Peacock, J. A. 1999, Cosmological Physics (Cambridge University Press)
Rush, B., Malkan, M. A., & Spinoglio, L. 1993, ApJS, 89, 1
Rybicki, G. B. & Hummer, D. G. 1991, A&A, 245, 171
Sanders, D. B. & Mirabel, I. F. 1996, ARA&A, 34, 749
Sanders, D. B., Soifer, B. T., Elias, J. H., Madore, B. F., Matthews, K., Neugebauer, G., & Scoville, N. Z. 1988, ApJ, 325, 74
Schmutz, W., Leitherer, C., & Gruenwald, R. 1992, PASP, 104, 1164
Smith, H. E., Lonsdale, C. J., Lonsdale, C. J., & Diamond, P. J. 1998, ApJ Lett., 493, L17+
Smith, L. J., Norris, R. P. F., & Crowther, P. A. 2002, MNRAS, 337, 1309

Appendix A: Simulation results

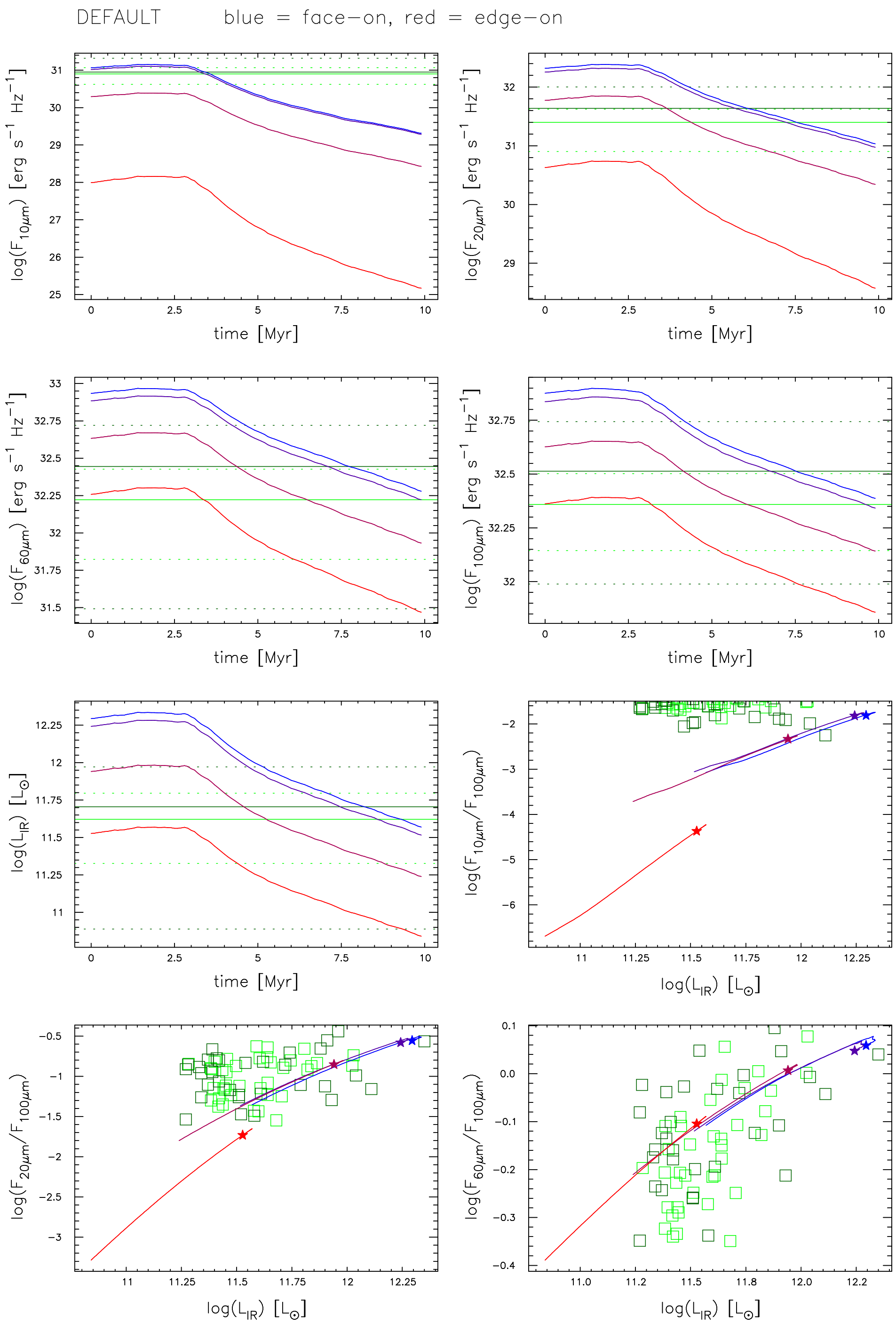

Fig. A.1. These panels show the infrared results of the simulation DEFAULT. The top 4 panels show the 10, 20, 60 and 100μm flux as a function of time. The fifth panel shows the calculated infrared luminosity through time. The last three panels give a more observational interpretation of the data. In these panels three IR colors (10μm/100μm, 20μm/100μm and 60μm/100μm) are plotted versus the IR luminosity. To indicate the evolution direction, the start of the track is marked with a star. All axes are logarithmic except the time axes. The simulation results are color coded from blue (indicating completely face-on) to red (completely edge-on). The two reference sets are added in green squares in the last 3 panels (light green : 12 micron galaxy sample (Rush et al., 1993), dark green : IRAS Bright Galaxy Sample (Condon et al., 1991)). In the first 5 panels, the solid lines represent the mean of these data sets and the dotted lines a 1 σ deviation.

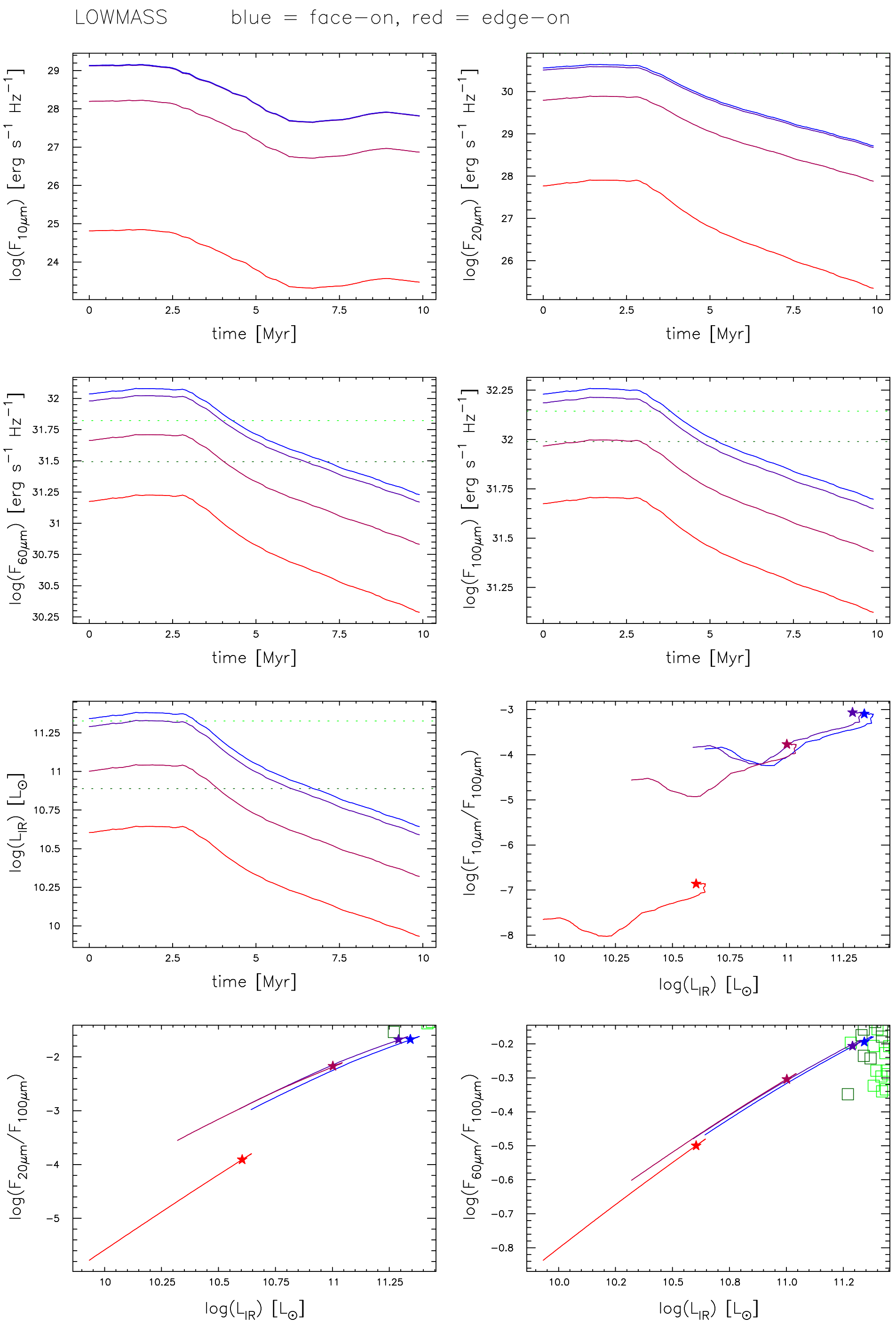

Fig. A.2. These panels show the infrared results of the simulation LOWMASS. The color coding is the same as in figure A.1

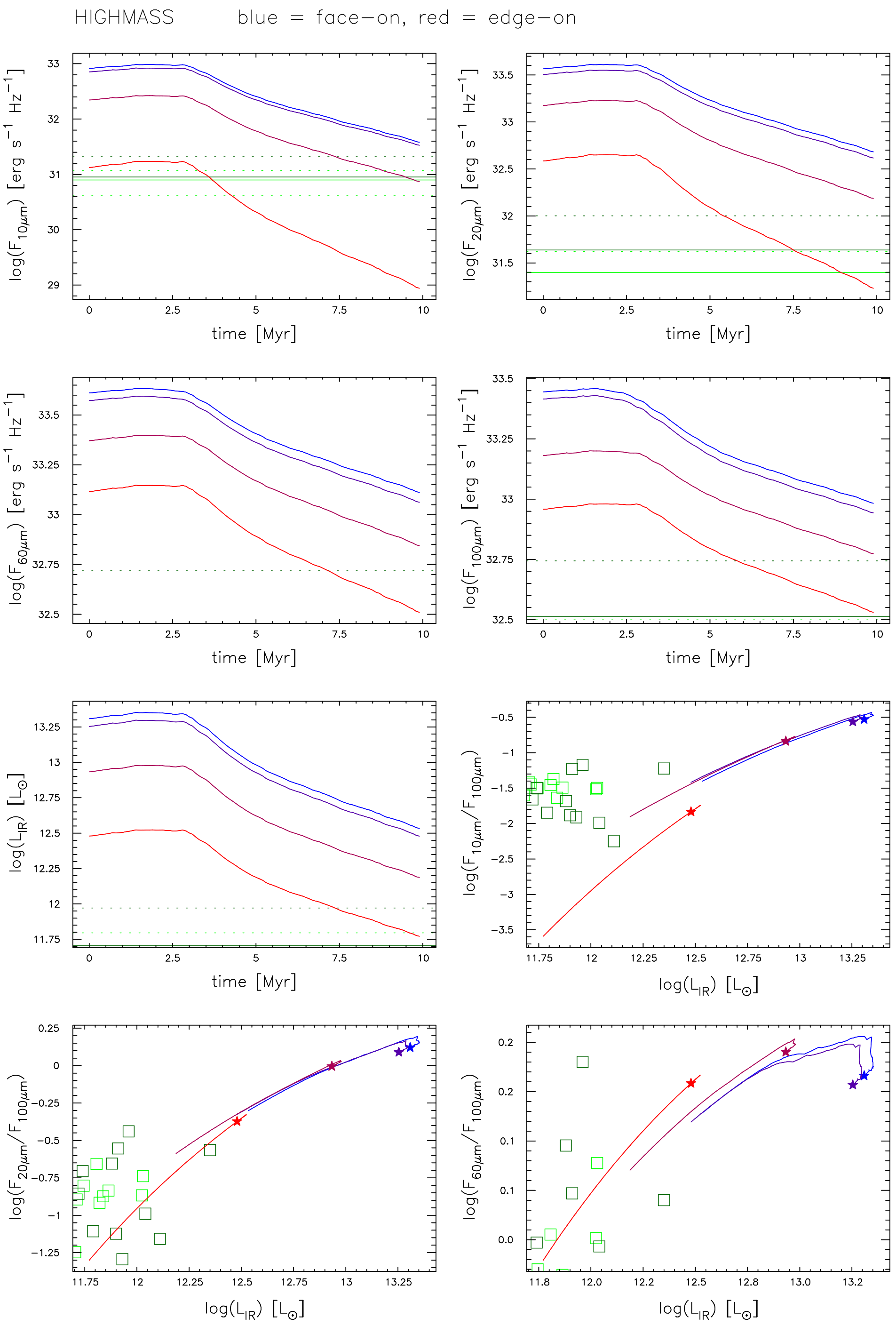

Fig. A.3. These panels show the infrared results of the simulation HIGHMASS. The color coding is the same as in figure A.1.

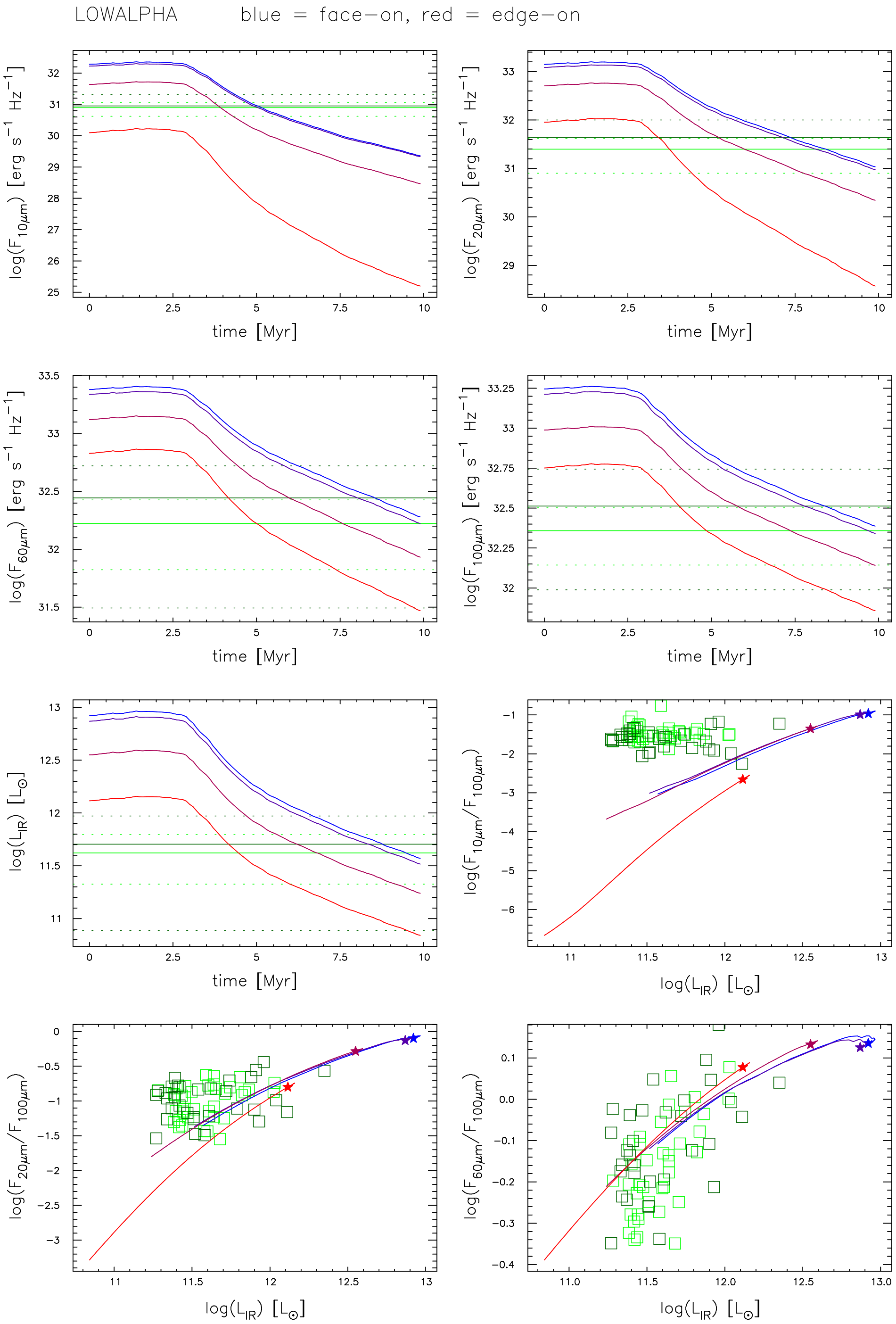

Fig. A.4. These panels show the infrared results of the simulation LOWALPHA. The color coding is the same as in figure A.1.

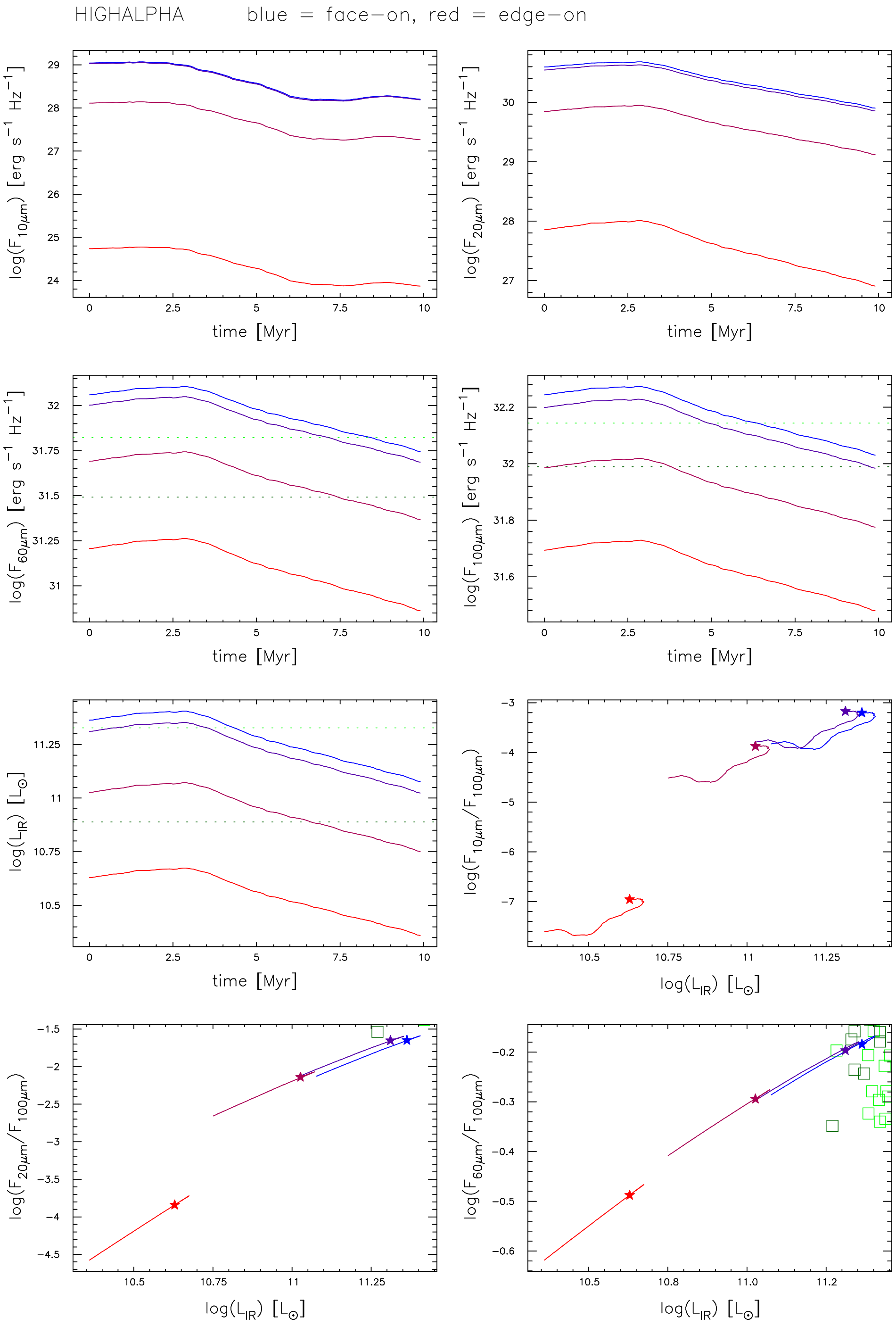

Fig. A.5. These panels show the infrared results of the simulation HIGHALPHA. The color coding is the same as in figure A.1.

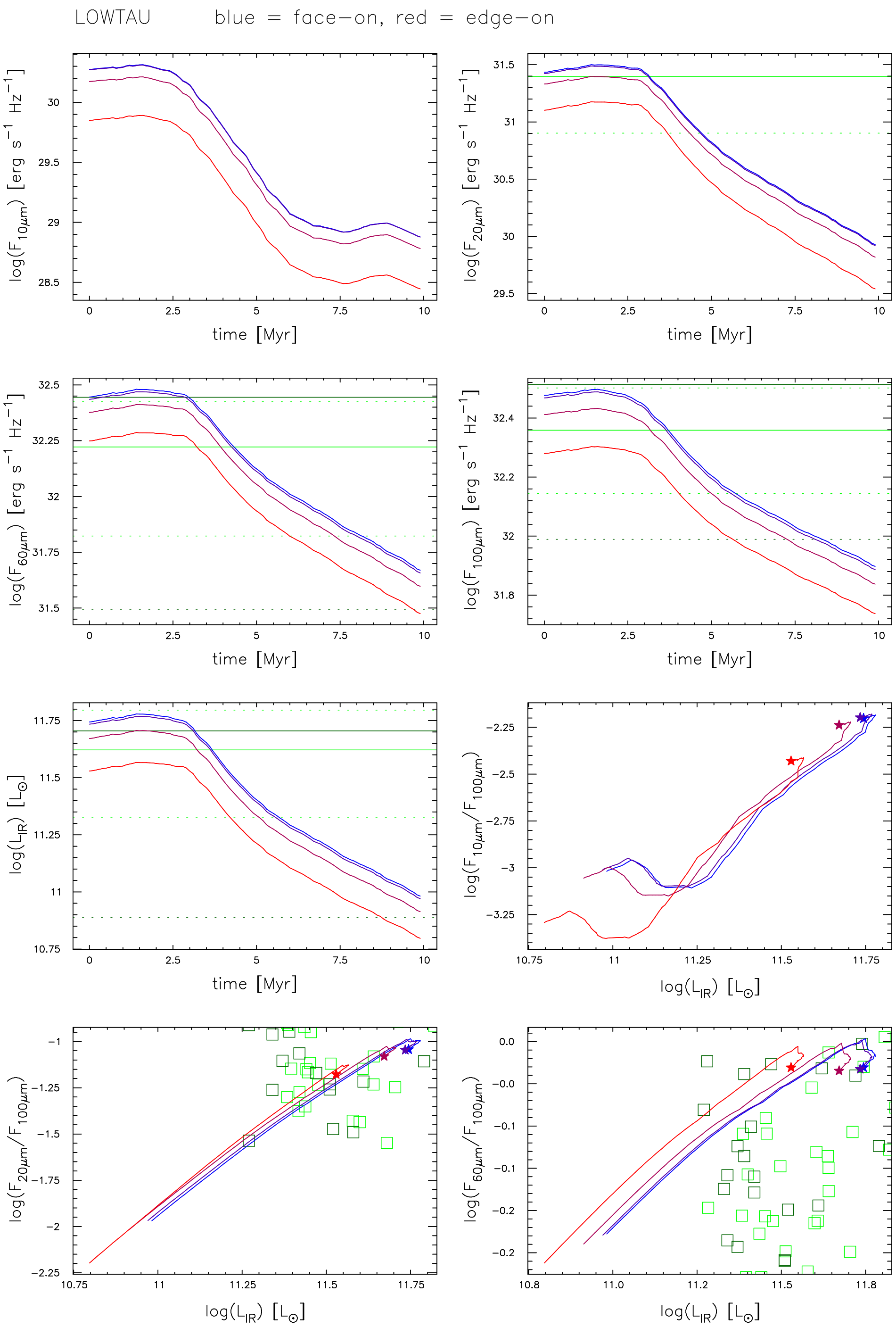

Fig. A.6. These panels show the infrared results of the simulation LOWTAU. The color coding is the same as in figure A.1.

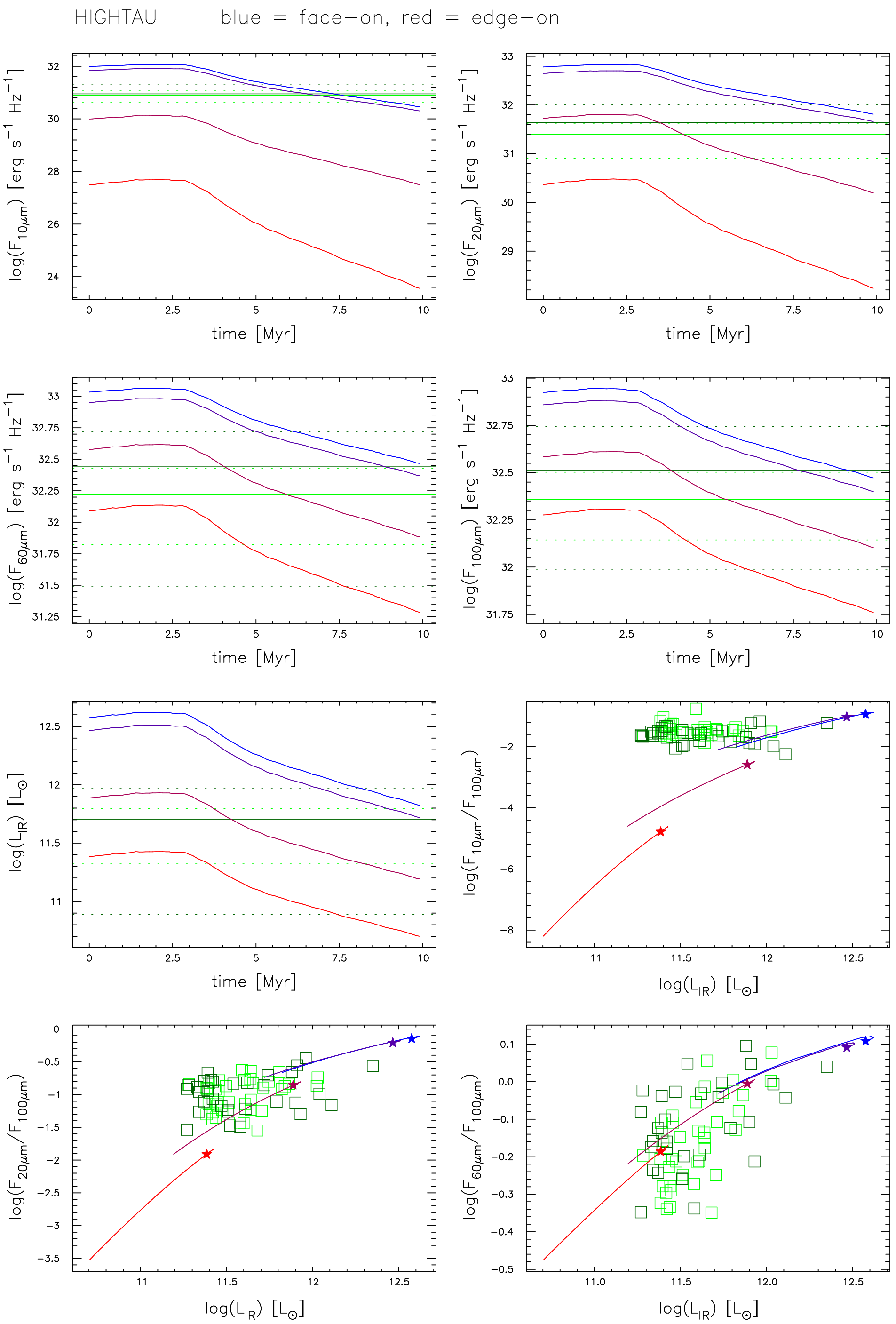

Fig. A.7. These panels show the infrared results of the simulation HIGHTAU. The color coding is the same as in figure A.1.

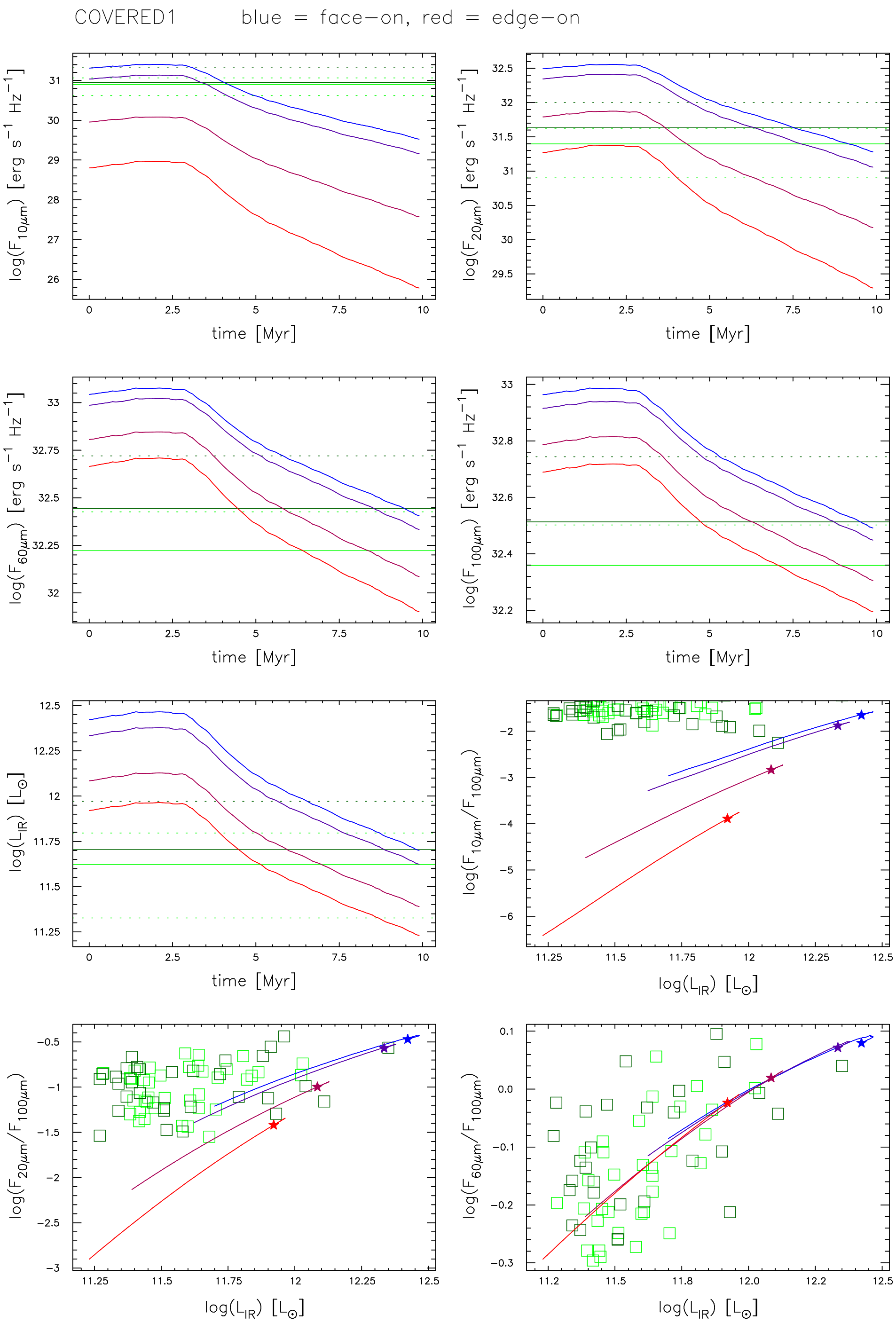

Fig. A.8. These panels show the infrared results of the simulation COVERED1. The color coding is the same as in figure A.1.

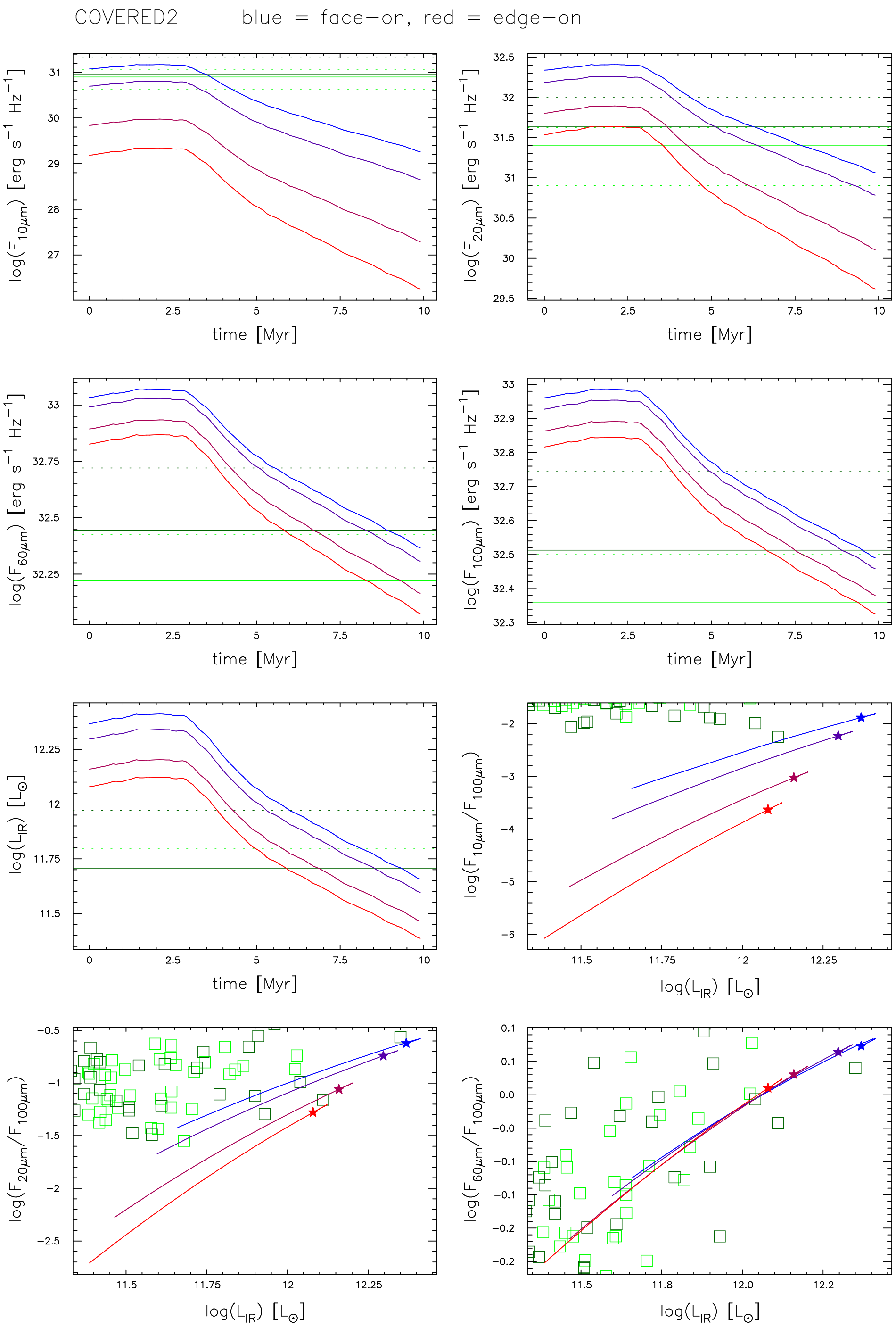

Fig. A.9. These panels show the infrared results of the simulation COVERED2. The color coding is the same as in figure A.1.

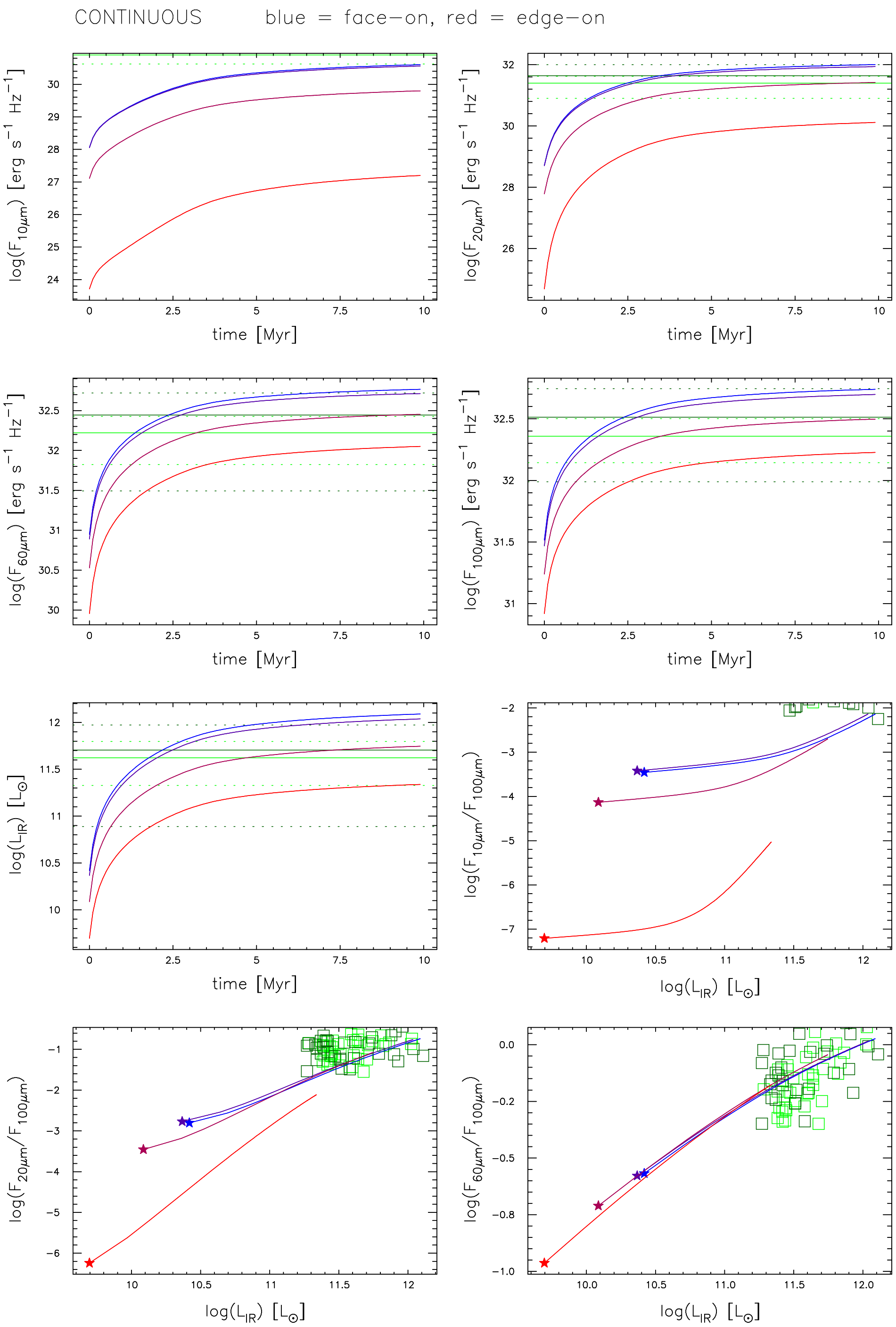

Fig. A.10. These panels show the infrared results of the simulation CONTINUOUS. The color coding is the same as in figure A.1.

Appendix B: Simulation comparison

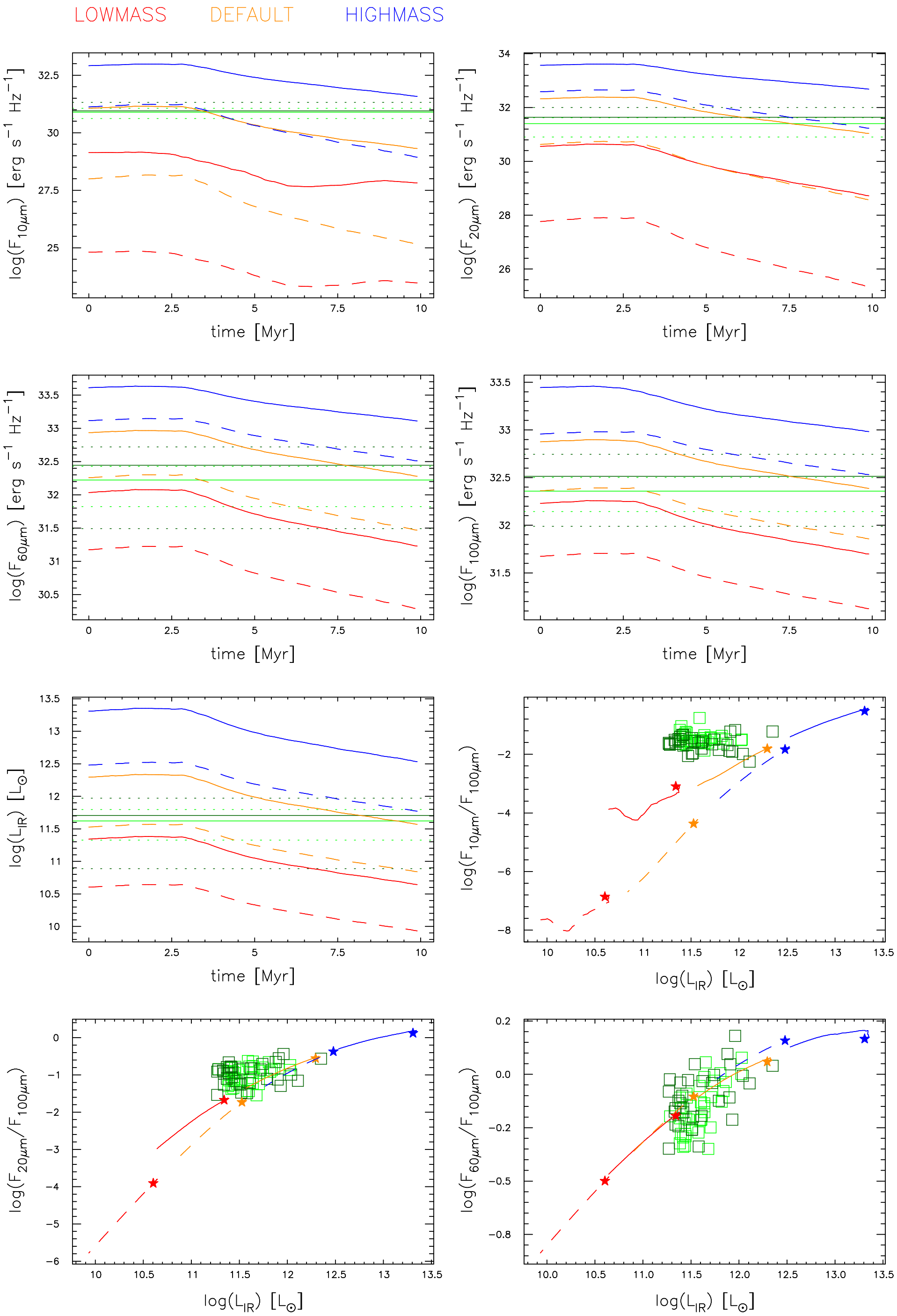

Fig. B.1. These panels show the influence of the starburst mass ($M_{\rm SB}$) on the infrared results. The two deviations are compared to the default value. The simulation results for the lowest deviation are indicated by red lines, the high deviation by blue lines and the default set is drawn in yellow. The solid lines are results for face-on observations, the dashed lines show the edge-on results. Like in figures A.1-A.7, the top 4 panels show the 10, 20, 60 and 100μm flux as a function of time, the fifth panel shows the calculated infrared luminosity through time and the last three panels show three IR colors (10μm/100μm, 20μm/100μm and 60μm/100μm) versus the IR luminosity. To indicate the evolution direction, the start of the track is marked with a star. All axes are logarithmic except the time axes. Again, the two reference sets are added in green squares in the last 3 panels (light green : 12 micron galaxy sample (Rush et al., 1993), dark green : IRAS Bright Galaxy Sample (Condon et al., 1991)). In the first 5 panels, the solid lines represent the mean of these data sets and the dotted lines a 1 σ deviation.

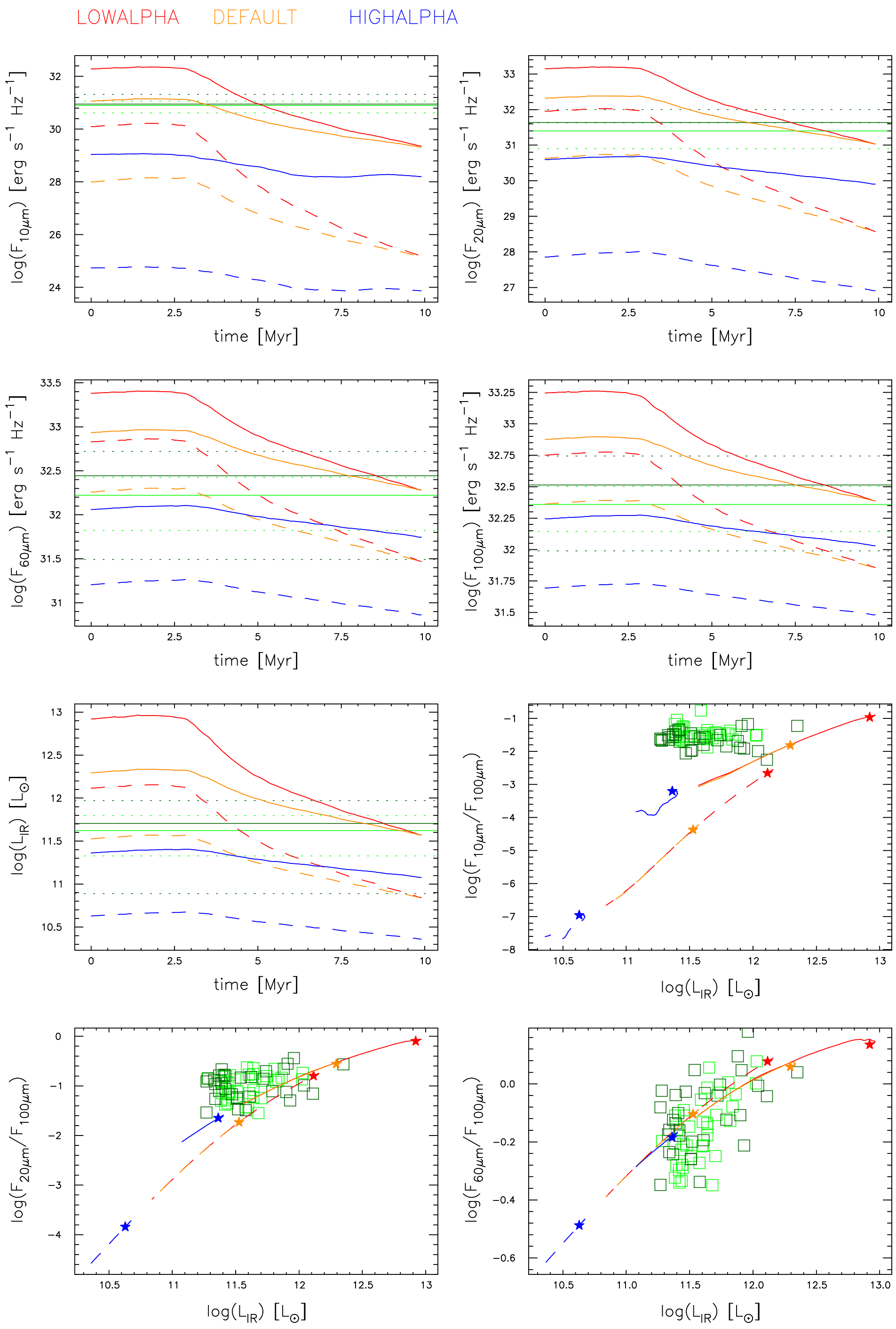

Fig. B.2. These panels show the influence of the IMF slope (α) on the infrared results. The color coding is the same as in figure B.1.

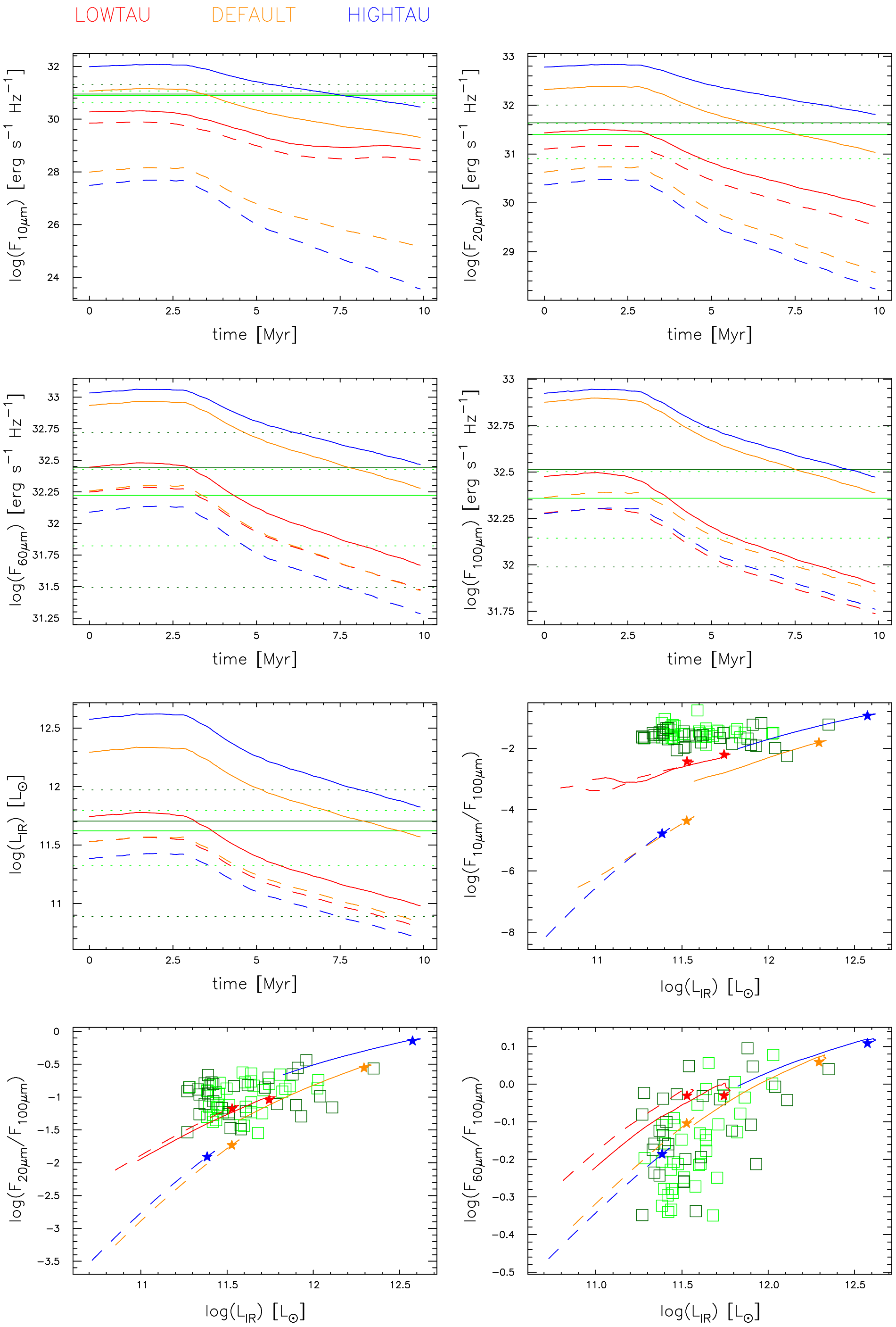

Fig. B.3. These panels show the influence of the dust density (τ) on the infrared results. The color coding is the same as in figure B.1.

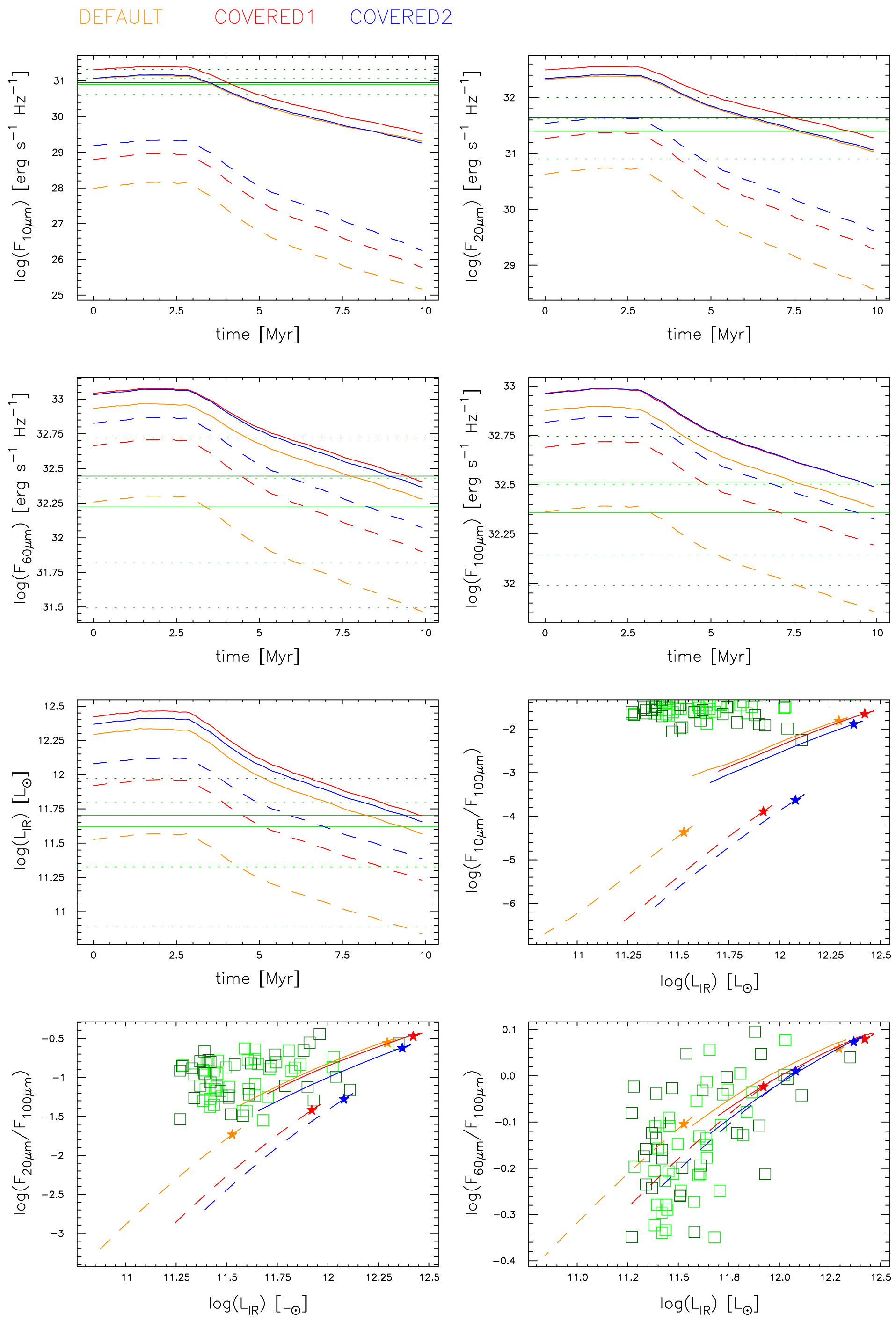

Fig. B.4. These panels show the influence of the closing angle (η) on the infrared results. The color coding is the same as in figure B.1. Note: for this simulation both deviation are higher than the default value. However the default is still indicated with yellow and the two deviations with red and blue.

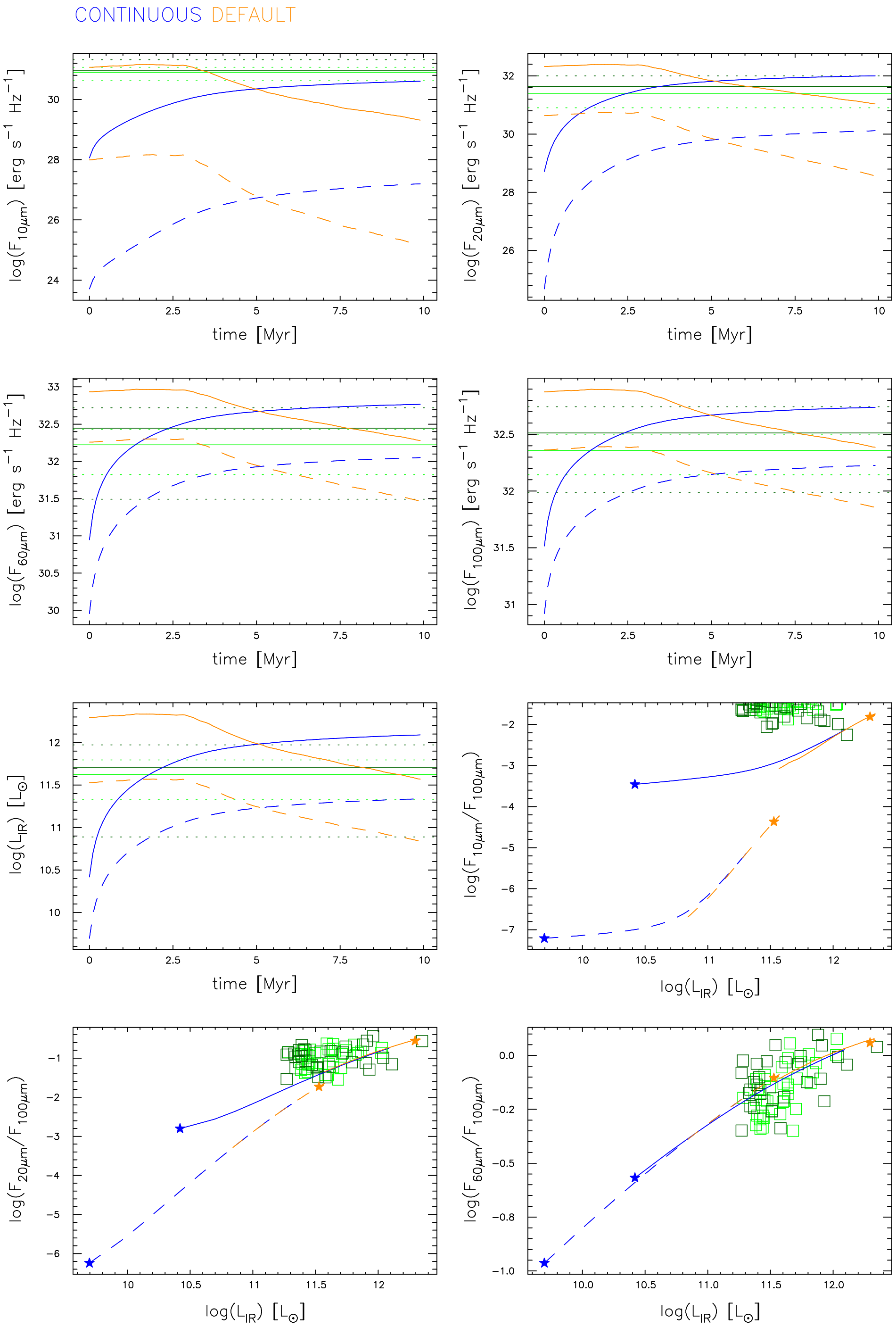

Fig. B.5. These panels show the influence of the star formation history on the infrared results. The color coding is the same as in figure B.1. Note: for this simulation there is only one deviation. The default is still indicated with yellow and the two deviations with red and blue.